



Polarimetric Hydrometeor Classification

Simulation of hydrometeor scattering properties

	In progress	In validation	Approved
Document status	<input checked="" type="checkbox"/>	<input type="checkbox"/>	<input type="checkbox"/>

Version 0.6

Document History

Responsible People

Creation/Edition	Jordi Figueras i Ventura
Revision	
Approval	
Further information	

Version Control

Version	Edited by	Date	Activity
0.1	Jordi Figueras i Ventura	04.04.2014	Creation
0.2	Jordi Figueras i Ventura	11.04.2014	DSD of rain
0.3	Jordi Figueras i Ventura	16.04.2014	Changes in ice crystals simulations
0.4	Jordi Figueras i Ventura	30.07.2014	Computation of fraction mass water. Various changes.
0.5	Jordi Figueras i Ventura	21.08.2014	Preliminary results. Various changes across the report
0.6	Jordi Figueras i Ventura	15.02.2023	Correction of errors in raindrop axis ratio and ice refractive index

Contents

Chapter 1	Introduction.....	7
Chapter 2	Polarimetric variables simulation.....	8
2.1	Polarimetric variables in terms of the scattering matrix elements.....	8
2.2	Canting angle.....	9
2.3	T-matrix computations.....	11
Chapter 3	Hydrometeor classification in the literature.....	16
3.1	Hydrometeor types.....	16
3.2	Classification techniques.....	17
3.3	Assumptions on microphysics.....	18
3.3.1	Assumptions on individual particles.....	19
3.3.2	Assumptions on particle size distributions.....	21
Chapter 4	The MeteoSwiss approach.....	24
Chapter 5	Simulations of Rain.....	25
5.1	Drop shape.....	25
5.2	Drop Size Distribution.....	25
5.3	Liquid water content.....	26
5.4	Rainfall rate.....	26
5.5	Refractive index.....	27
Chapter 6	Simulation of ice crystals.....	28
6.1	Particle shape.....	28
6.2	Particle size distribution.....	30
6.3	Equivalent liquid water content.....	31
6.4	Equivalent rainfall rate.....	31
6.5	Refractive index.....	32
Chapter 7	Simulations of aggregates (Dry Snow).....	34
7.1	Particle shape.....	34
7.2	Particle Size Distribution.....	34
7.3	Equivalent liquid water content.....	35
7.4	Equivalent rainfall rate.....	35
7.5	Refractive index.....	35
Chapter 8	Simulations of wet snow.....	36
8.1	Particle shape.....	36
8.2	Particle size distribution.....	36
8.3	Equivalent liquid water content.....	36
8.4	Equivalent rainfall rate.....	36
8.5	Mass water fraction.....	37
8.6	Refractive index.....	39
Chapter 9	Simulations of hail/melting hail.....	41
9.1	Particle shape.....	41
9.2	Particle size distribution.....	42
9.3	Equivalent liquid water content.....	42
9.4	Equivalent rainfall rate.....	42
9.5	Mass water fraction.....	43

9.6	Refractive index.....	44
9.7	Vertical column.....	44
Chapter 10	Simulation of graupel/melting graupel.....	45
10.1	Particle shape.....	45
10.2	Particle size distribution.....	45
10.3	Equivalent liquid water content.....	45
10.4	Equivalent rainfall rate.....	45
10.5	Refractive index.....	45
Chapter 11	Simulation results.....	46
11.1	Single particle scattering.....	46
11.1.1	Ice crystals.....	46
11.1.2	Dry snow.....	47
11.1.3	Wet snow.....	48
11.1.4	Rain.....	49
11.1.5	Graupel.....	50
11.1.6	Hail.....	51
11.2	Bulk hydrometeor scattering.....	53
11.2.1	Ice crystals.....	53
11.2.2	Dry snow.....	55
11.2.3	Wet snow.....	56
11.2.4	Rain.....	58
11.2.5	Graupel.....	59
11.2.6	Hail.....	60
11.3	Membership Functions.....	62
Chapter 12	References.....	63

Figures

Fig. 1 Reference system in Holt (1984).....	12
Fig. 2 Reference system in Mischenko (2000).....	13
Fig. 3 Distribution of ice particles as a function of temperature and supersaturation.....	29
Fig. 4 Concentration and slope parameters for truncated exponential PSDs plotted against surface air temperature.....	34
Fig. 5 Scattering properties of individual ice crystals at -30°C (spherical particles).....	46
Fig. 6 Scattering properties of individual ice crystals at -20°C (Hexagonal plates).....	47
Fig. 7 Scattering properties of individual ice crystals at -15°C (dendrites).....	47
Fig. 8 Scattering properties of individual snowflakes.....	48
Fig. 9 Scattering properties of individual melting snowflakes at 0.5°C.....	48
Fig. 10 Scattering properties of individual melting snowflakes at 1.5°C.....	49
Fig. 11 Scattering properties of individual raindrops at 3°C.....	49

Fig. 12 Scattering properties of individual raindrops at 30°C.....	50
Fig. 13 Scattering properties of individual graupel at 0°C (no melting).....	50
Fig. 14 Scattering properties of individual graupel at 3°C.....	51
Fig. 15 Scattering properties of individual graupel at 6°C.....	51
Fig. 16 Scattering properties of individual hailstones at 0°C (no melting).....	52
Fig. 17 Scattering properties of individual hailstones at 6°C.....	52
Fig. 18 Scattering properties of individual hailstones at 15°C.....	53
Fig. 19 Scattering properties of individual hailstones at 24°C.....	53
Fig. 20 Bulk scattering properties of ice crystals (different crystal habits put together).....	54
Fig. 21 Relationship between equivalent rainfall rate and polarimetric parameters for ice crystals.....	55
Fig. 22 Bulk scattering properties of dry snow.....	55
Fig. 23 Relationship between equivalent rainfall rate and polarimetric parameters for dry snow.....	56
Fig. 24 Bulk scattering properties of wet snow.....	57
Fig. 25 Relationship between polarimetric variables and equivalent rainfall rate for wet snow.....	57
Fig. 26 Bulk scattering properties of rain.....	58
Fig. 27 Relationship between rainfall rate and polarimetric variables.....	59
Fig. 28 Bulk scattering properties of graupel.....	60
Fig. 29 Relationship between equivalent rainfall rate and polarimetric variables for graupel.....	60
Fig. 30 Bulk scattering properties of hail.....	61
Fig. 31 Relationship between equivalent rainfall rate and polarimetric variables for hail.....	61
Fig. 32 Membership functions for the elevation 2 (0.4°) and 20 (40°) of the MeteoSwiss volumetric scan. Color code from black, bluish, green, orange: rain, snow, melting snow, ice crystals, hail/melting hail and graupel/melting graupel.....	62

Tables

Table 1 Hydrometeor types according to different authors.....	17
Table 2 Use of variables in hydrometeor classification.....	18
Table 3 Assumed microphysics of particles by Dolan and Rutledge (2009).....	19
Table 4 Assumed microphysics of particles by Dolan et al (2013).....	20
Table 5 Assumed microphysics of particles by Marzano et al (2007).....	20

Table 6 Assumed microphysics of particles by Marzano et al (2010).....	20
Table 7 Assumed microphysics of particle size distributions by Dolan and Rutledge (2009).....	22
Table 8 Assumed microphysics of particle size distributions by Dolan et al (2013).....	22
Table 9 Assumed microphysics of particle size distribution by Marzano et al (2007).....	23
Table 10 Assumed microphysics of particle size distribution by Marzano et al (2010).....	23
Table 11 Coefficients of the minor-major dimension relationship.....	28
Table 12 Coefficients of the mass-major dimension relation.....	31
Table 13 Area ratio of various shapes.....	32
Table 14 Coefficients of the density-major dimension relation.....	33

Chapter 1 **Introduction**

MeteoSwiss is currently developing an hydrometeor classification algorithm based primarily on polarimetric weather radar data and temperature information from the numerical weather prediction COSMO-2 model.

The new algorithm is based on fuzzy logic. The first step in the creation of the algorithm is to construct realistic membership functions that relate each hydrometeor type with the expected polarimetric variables values. The approach followed is to perform scattering simulations, using the Mischenko T-matrix code, of each hydrometeor type based on a set of realistic assumptions. This report explains the methodology for the simulations and the assumptions on the characteristics of the hydrometeors.

The report is structured as follows: Chapter 2 defines the polarimetric variables in terms of the scattering matrix. Chapter 3 is a review of the assumptions existing in literature. Chapter 4 explains the philosophy of the MeteoSwiss hydrometeor classification. The rest of the chapters provide details on the assumptions for each hydrometeor.

Chapter 2 Polarimetric variables simulation

2.1 Polarimetric variables in terms of the scattering matrix elements

Here we formalize the polarimetric variables in terms of the elements of the scattering matrix. More details can be found in Bringi and Chandrasekar (2001).

The incident and scattered electric fields are related by the scattering matrix:

$$\begin{pmatrix} E_{vs} \\ E_{hs} \end{pmatrix} = \frac{e^{jk_o r}}{r} \begin{pmatrix} S_{11} & S_{12} \\ S_{21} & S_{22} \end{pmatrix} \begin{pmatrix} E_{vi} \\ E_{hi} \end{pmatrix} \quad (1)$$

The polarimetric variables are computed from the elements of the forward and backward scattering matrixes. The backward scattering matrix can be written as:

$$S_b = \begin{pmatrix} S_{b11} & S_{b12} \\ S_{b21} & S_{b22} \end{pmatrix} [m] \quad (2)$$

While the forward scattering matrix is:

$$S_f = \begin{pmatrix} S_{f11} & S_{f12} \\ S_{f21} & S_{f22} \end{pmatrix} [m] \quad (3)$$

The elements of the scattering matrix are dependent only on the shape, size, orientation and refractive index of the particle and the incident and scattered angles of the signal.

From the backward scattering matrix we can compute the backscatter cross section for a single particle as:

$$\sigma_{bx} = 4\pi |S_{bxx}|^2 [m^2] \quad (4)$$

Where the subscript x stands for horizontal or vertical polarization. From the forward scattering matrix the extinction cross section can be computed as:

$$\sigma_{ex} = \frac{4\pi}{1000 k_o} I\{S_{fxx}\} [m^2]; k_o = \frac{2\pi}{\lambda} \quad (5)$$

Where λ is the radar wavelength in mm.

The radar return is actually the combination of the scattering of multiple particles of different sizes in the radar resolution volume. Assuming they are all equally oriented the reflectivity can be computed as:

$$Z_x = \frac{\lambda^4}{\pi^5} \frac{1}{|K_w|^2} 10^6 \int N(D) \sigma_{bx}(D) dD \left[\frac{mm^6}{m^3} \right] \quad (6)$$

Where $N(D)$ is the particle size distribution (PSD) and $|K_w|^2$ is the dielectric factor defined as:

$$|K_w|^2 = \left| \frac{\epsilon_r - 1}{\epsilon_r + 2} \right|^2 \quad (7)$$

Where ϵ_r is the complex dielectric constant. The relation between dielectric constant and refractive index N can be approximated as:

$$N = \sqrt{\epsilon_r \mu_r} \approx \sqrt{\epsilon_r} \quad (8)$$

Since for most materials the permittivity μ_r is approximately one. Therefore:

$$\epsilon_r = \epsilon_1 + j\epsilon_2 \approx N^2 = (n + jk)^2 \quad (9)$$

Where:

$$n = \sqrt{\frac{\sqrt{\epsilon_1^2 + \epsilon_2^2} + \epsilon_1}{2}} \quad (10)$$

And:

$$k = \sqrt{\frac{\sqrt{\epsilon_1^2 + \epsilon_2^2} - \epsilon_1}{2}} \quad (11)$$

In a similar manner the specific attenuation is defined as:

$$A_x = 4.34 \cdot 10^3 \int N(D) \sigma_{ex}(D) dD \left[\frac{dB}{km} \right] \quad (12)$$

The linear depolarization ratio is:

$$LDR = 10 \log \frac{\int N(D) |S_{bhv}(D)|^2 dD}{\int N(D) |S_{bhh}(D)|^2 dD} [dB] \quad (13)$$

The specific differential phase is:

$$KDP = \frac{180}{\pi} \frac{\lambda}{10^3} 10^3 \int N(D) R \{ S_{fhh}(D) - S_{fvv}(D) \} dD \left[\frac{mm^6}{m^3} \right] \quad (14)$$

The backscatter co-polar differential phase is:

$$\delta_{co} = \arg \left\{ \int N(D) S_{bhh}(D) S_{bvv}^*(D) dD \right\} \frac{180}{\pi} [^\circ] \quad (15)$$

And the co-polar correlation coefficient is:

$$\rho_{hv} = \left| \frac{\int N(D) S_{bhh}(D) S_{bvv}^*(D) dD}{\int N(D) |S_{bhh}(D)|^2 dD \int N(D) |S_{bvv}(D)|^2 dD} \right| = \frac{4\lambda^4}{\pi^4 |K_w|^2} 10^6 \frac{\left| \int N(D) S_{bhh}(D) S_{bvv}^*(D) dD \right|}{\sqrt{Z_h^{lin} Z_v^{lin}}} \quad (16)$$

2.2 Canting angle

According to Huang et al. (2008) the orientation of the particle shape (if rotationally symmetric) is defined by two orientation angles β (from the zenith) and α (from the azimuth). Assuming that α and β are independent variables the orientation distribution is described by the probability that the symmetry axis lies between the solid angle Ω and $\Omega + d\Omega$ on a spherical surface, which can be written as:

$$p_{\Omega}(\alpha, \beta) = p(\beta) \sin\beta p(\alpha) \quad (17)$$

The probability of α should be uniform between $[0, 2\pi]$. In such case:

$$p_{\Omega}(\alpha, \beta) = \frac{1}{2\pi} p_{\Omega}(\beta) \quad (18)$$

The probability density distribution function of p_{Ω} is a special case of the general Fisher distribution valid for describing statistics on a spherical surface, given by:

$$p_{\Omega}(\beta) = \frac{k e^{k \cos\beta}}{4\pi \sinh(k)} \sin\beta = p(\beta) \sin\beta \quad (19)$$

Most authors consider only the canting angle given by β and assume that $\tan\beta$ has a Gaussian probability density function. When β is small, β and $\tan\beta$ have similar probability. There is an approximate relation between k and the standard deviation of the Gaussian form of $p(\beta)$.

Now, Due to the randomness of their orientation, drops with the same size may have a different backscatter and forward scatter matrix. Therefore the drop distribution is now not only dependent on the size but also on the orientation. For example, the reflectivity can be expressed as:

$$Z_x = \frac{\lambda^4}{\pi^5} \frac{1}{|K_w|^2} 10^6 \int \sum_{i=1}^{N(D)} \sigma_{bx}(D, \alpha_i, \beta_i) dD \left[\frac{mm^6}{m^3} \right] \quad (20)$$

Where α and β are random variables defining the orientation. Since $N(D)$ is a density and therefore can be less than unity (i.e. less than one drop in 1 cubic meter). The accuracy of the result can be increased by arbitrary increasing the size of the volume, i.e:

$$Z_x = \frac{\lambda^4}{\pi^5} \frac{1}{|K_w|^2} 10^6 \int \frac{1}{L} \sum_{i=1}^{N(D)L} \sigma_{bx}(D, \alpha_i, \beta_i) dD \left[\frac{mm^6}{m^3} \right] \quad (21)$$

Now, since α and β are random variables, the scattering matrix can be seen as the result of a random process and consequently the polarimetric variables can also be considered a random process and we can characterize them by their mean and standard deviation. The sample mean can be written as:

$$\bar{x} = \frac{1}{M} \sum_{i=1}^M x_i \quad (22)$$

While the sample standard deviation can be written as:

$$\sigma_x = \sqrt{\frac{1}{M} \sum_{i=1}^M (x_i - \bar{x})^2} = \sqrt{\left(\frac{1}{M} \sum_{i=1}^M x_i^2 \right) - \bar{x}^2} \quad (23)$$

Therefore, as an example, the mean reflectivity for a particular DSD can be computed as:

$$\begin{aligned} \bar{Z}_x &= \frac{1}{M} \sum_{j=1}^M \frac{\lambda^4}{\pi^5 |K_w|^2} 10^6 \int \frac{1}{L} \sum_{i=1}^{N(D)L} \sigma_{bx}(D, \alpha_{i,j}, \beta_{i,j}) dD \\ \textcolor{red}{i} \frac{1}{M} \frac{\lambda^4}{\pi^5 |K_w|^2} 10^6 \int \sum_{j=1}^M \frac{1}{L} \sum_{i=1}^{N(D)L} \sigma_{bx}(D, \alpha_{i,j}, \beta_{i,j}) dD & \quad (24) \end{aligned}$$

Whereas the standard deviation can be computed as:

$$\begin{aligned} \sigma_{z_x} &= \sqrt{\frac{1}{M} \sum_{j=1}^M \left(\frac{\lambda^4}{\pi^5 |K_w|^2} 10^6 \int \frac{1}{L} \sum_{i=1}^{N(D)L} \sigma_{bx}(D, \alpha_{i,j}, \beta_{i,j}) dD \right)^2 - \bar{Z}_x^2} = \textcolor{red}{i} \\ \textcolor{red}{i} \sqrt{\frac{1}{M} \left(\frac{\lambda^4}{\pi^5 |K_w|^2} 10^6 \right)^2 \sum_{j=1}^M \left(\int \frac{1}{L} \sum_{i=1}^{N(D)L} \sigma_{bx}(D, \alpha_{i,j}, \beta_{i,j}) dD \right)^2 - \bar{Z}_x^2} & \quad (25) \end{aligned}$$

With M sufficiently large. Here α and β are randomly generated, α following a uniform distribution between 0 and 360 and β a Gaussian distribution with 0 mean and standard deviation depending on the type (and eventually size) of the particle.

To compute the standard deviation of non-linear functions, such as the logarithms, perturbation analysis can be used (provided the variables have a narrow distribution about their mean):

$$\sigma_{x_{dB}} = 10 \log_{10} \left(1 + \frac{\sigma_{x_{lin}}}{\bar{x}_{lin}} \right) \quad (26)$$

2.3 T-matrix computations

We assume that the incident wave is propagating along the positive axis: $\phi_o=0^\circ$, $\theta_o=90-\theta_e$. The forward scattering is therefore along the same direction ($\phi_f=0^\circ$, $\theta_f=90-\theta_e$) while the backward scattering is in the opposite direction ($\phi_b=180^\circ$, $\theta_b=90+\theta_e$).

According to Holt (1984) the scattering matrix of an individual spheroid can be written as:

$$S = \begin{pmatrix} S_{11} \cos^2 \alpha + S_{22} \sin^2 \alpha & (S_{11} - S_{22}) \cos \alpha \sin \alpha \\ (S_{11} - S_{22}) \cos \alpha \sin \alpha & S_{11} \sin^2 \alpha + S_{22} \cos^2 \alpha \end{pmatrix} \quad (27)$$

With S_{11} and S_{22} the vertical and horizontal scattering coefficients in the reference frame of the incident wave.

In the same paper the following approximation is used:

$$S_{11} = f_a \sin^2 \psi + f_b \cos^2 \psi \quad (28)$$

$$S_{22} = f_b \quad (29)$$

Where f_a is the scattering amplitude if the electric field vector is parallel to the symmetry axis of the hydrometeor and f_b is the scattering amplitude if the electric field is perpendicular to the symmetry axis. The authors state that, for forward scattering these approximations apply, in rain, for frequencies up to 137 GHz whereas for backward scattering they hold valid up to 30 GHz provided a low elevation angle.

Using the trigonometric identity:

$$\sin^2 \alpha + \cos^2 \alpha = 1 \quad (30)$$

And equations 28 and 29, Eq. 27 can be re-written as:

$$S = \begin{pmatrix} (f_a - f_b) \sin^2 \psi \cos^2 \alpha + f_b & (f_a - f_b) \sin^2 \psi \sin \alpha \cos \alpha \\ (f_a - f_b) \sin^2 \psi \sin \alpha \cos \alpha & (f_a - f_b) \sin^2 \psi \sin^2 \alpha + f_b \end{pmatrix} \quad (31)$$

The same paper shows the following angular relations:

$$\cos \psi = \cos \theta \sin \chi - \sin \theta \cos \chi \cos \phi \quad (32)$$

$$\cos \alpha \sin \psi = \cos \theta \cos \chi + \sin \theta \sin \chi \cos \phi \quad (33)$$

$$\sin \alpha \sin \psi = \sin \theta \sin \phi \quad (34)$$

Consequently, the scattering matrix can be written in terms of the orientation angles of the particle as:

$$S = \begin{pmatrix} (f_a - f_b)(\cos \theta \cos \chi + \sin \theta \sin \chi \cos \phi)^2 + f_b & (f_a - f_b)(\cos \theta \cos \chi + \sin \theta \sin \chi \cos \phi)(\sin \theta \sin \phi) \\ (f_a - f_b)(\cos \theta \cos \chi + \sin \theta \sin \chi \cos \phi)(\sin \theta \sin \phi) & (f_a - f_b) \sin^2 \theta \sin^2 \phi + f_b \end{pmatrix} \quad (35)$$

Here the angles are defined as follows (see Fig. 1) :

- θ is the particle orientation angle formed by the true vertical (OZ) and the symmetry axis
- ϕ is the particle orientation angle formed by OX and the projection of the symmetry axis into the horizontal plane (OXY).
- χ is the incident wave elevation angle formed by the horizontal plane (OXY) and the direction of propagation of the incident wave.
- ψ is the angle between the symmetry axis of the particle and the direction of propagation of the incident wave.
- α is the angle between the vertical polarization field vector and the projection of the symmetry axis into the polarization plane

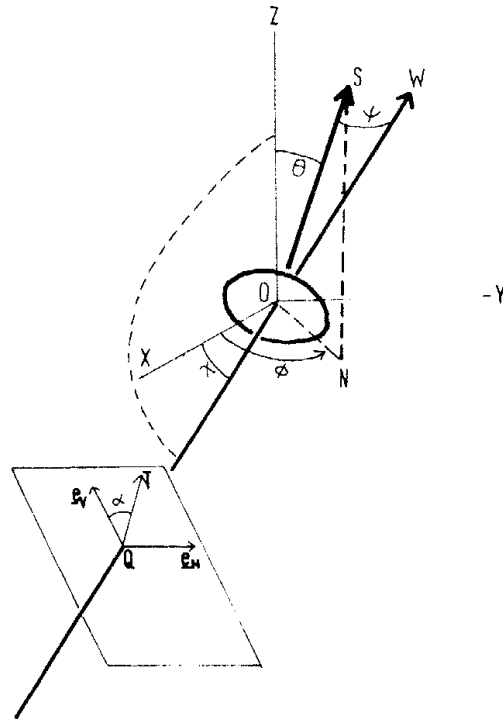


Fig. 1 Reference system in Holt (1984)

Mischenko (2000) uses a slightly different notation and reference framework (See Fig. 2):

- θ in Holt is β in Mischenko
- ϕ in Holt is α in Mischenko. However in Mischenko α is defined as the angle from YO to the line of nodes. However for rotationally symmetric bodies $\phi = \alpha$
- χ in Holt is θ_o in Mischenko. However in Mischenko θ is defined from ZO. Therefore $\theta_o - 90^\circ = \chi$

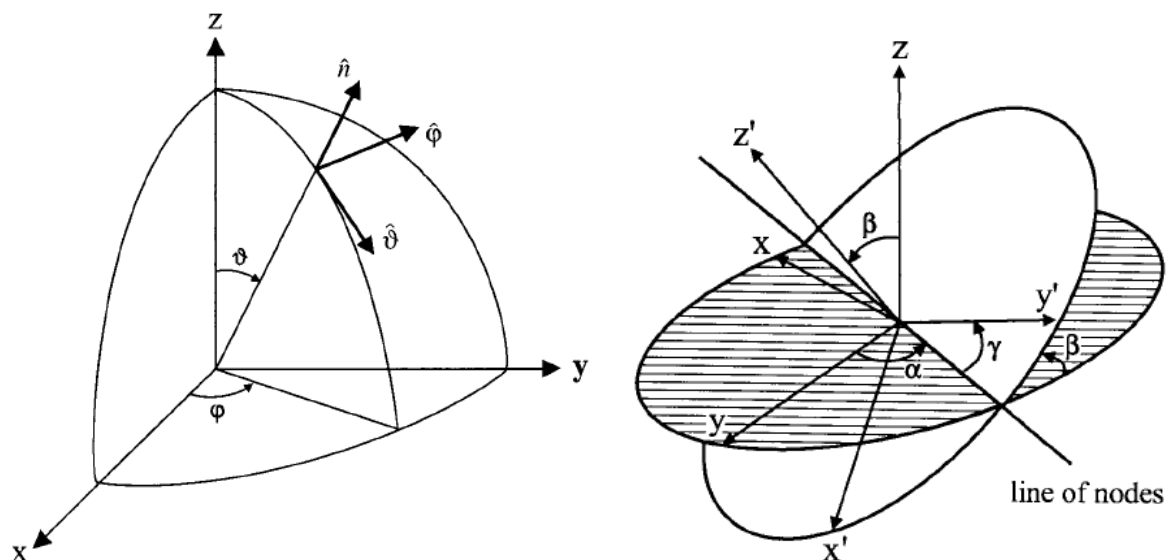


Fig. 2 Reference system in Mischenko (2000)

Now, considering the following trigonometric identities:

$$\cos(a \pm b) = \cos a \cos b \mp \sin a \sin b \quad (36)$$

$$\sin(a \pm b) = \sin a \cos b \pm \cos a \sin b \quad (37)$$

Eq. 35 in the Mischenko notation can be re-written as:

$$S = \begin{pmatrix} (f_a - f_b)(\cos \beta \sin \theta_o - \sin \beta \cos \theta_o \cos \alpha)^2 + f_b & (f_a - f_b)(\cos \beta \sin \theta_o + \sin \beta \cos \theta_o \cos \alpha)(\sin \beta \sin \alpha) \\ (f_a - f_b)(\cos \beta \sin \theta_o - \sin \beta \cos \theta_o \cos \alpha)(\sin \beta \sin \alpha) & (f_a - f_b) \sin^2 \beta \sin^2 \alpha + f_b \end{pmatrix} \quad (38)$$

From the scattering matrix in eq. 31 the following relations can be obtained:

$$|S_{hh}|^2 = |f_b|^2 - 2R\{f_b^i(f_b - f_a)\} \sin^2 \psi \sin^2 \alpha + |f_b - f_a|^2 \sin^4 \psi \sin^4 \alpha \quad (39)$$

$$|S_{vv}|^2 = |f_b|^2 - 2R\{f_b^i(f_b - f_a)\} \sin^2 \psi \cos^2 \alpha + |f_b - f_a|^2 \sin^4 \psi \cos^4 \alpha \quad (40)$$

$$I\{S_{hh}\} = I\{f_b\} - I\{f_b - f_a\} \sin^2 \psi \sin^2 \alpha \quad (41)$$

$$I\{S_{vv}\} = I\{f_b\} - I\{f_b - f_a\} \sin^2 \psi \cos^2 \alpha \quad (42)$$

$$|S_{hv}|^2 = |f_b - f_a|^2 \sin^4 \psi \sin^2 \alpha \cos^2 \alpha \quad (43)$$

$$R\{S_{hh} - S_{vv}\} = R\{f_b - f_a\} \sin^2 \psi \cos 2\alpha \quad (44)$$

$$S_{hh}^i S_{vv} = |f_b|^2 + |f_b - f_a|^2 \sin^4 \psi \sin^2 \alpha \cos^2 \alpha - f_b^i(f_b - f_a) \sin^2 \psi \cos^2 \alpha - f_b(f_b^i - f_a^i) \sin^2 \psi \sin^2 \alpha \quad (45)$$

In compact form:

$$|S_{hh}|^2 = |f_b|^2 - 2R\{f_b^i(f_b - f_a)\} A_2 + |f_b - f_a|^2 A_4 \quad (46)$$

$$|S_{vv}|^2 = |f_b|^2 - 2R\{f_b^i(f_b - f_a)\} A_1 + |f_b - f_a|^2 A_3 \quad (47)$$

$$I\{S_{hh}\} = I\{f_b\} - I\{f_b - f_a\} A_2 \quad (48)$$

$$I\{S_{vv}\} = I\{f_b\} - I\{f_b - f_a\} A_3 \quad (49)$$

$$|S_{hv}|^2 = |f_b - f_a|^2 A_5 \quad (50)$$

$$R\{S_{hh} - S_{vv}\} = R\{f_b - f_a\} A_7 \quad (51)$$

$$S_{hh}^i S_{vv} = |f_b|^2 + |f_b - f_a|^2 A_5 - f_b^i(f_b - f_a) A_1 - f_b(f_b^i - f_a^i) A_2 \quad (52)$$

Where:

$$A_1 = \sin^2 \psi \cos^2 \alpha \quad (53)$$

$$A_2 = \sin^2 \psi \sin^2 \alpha \quad (54)$$

$$A_3 = \sin^4 \psi \cos^4 \alpha \quad (55)$$

$$A_4 = \sin^4 \psi \sin^4 \alpha \quad (56)$$

$$A_5 = \sin^4 \psi \sin^2 \alpha \cos^2 \alpha \quad (57)$$

$$A_7 = \sin^2 \psi \cos 2\alpha \quad (58)$$

In terms of the orientation angles of the particle and the elevation angle of the incident wave the expressions A_1 to A_7 can be written as:

$$A_1 = (\cos \theta \cos \chi + \sin \theta \sin \chi \cos \phi)^2 \quad (59)$$

$$A_2 = \sin^2 \theta \sin^2 \phi \quad (60)$$

$$A_3 = (\cos \theta \cos \chi + \sin \theta \sin \chi \cos \phi)^4 \quad (61)$$

$$A_4 = \sin^4 \theta \sin^4 \phi \quad (62)$$

$$A_5 = (\cos \theta \cos \chi + \sin \theta \sin \chi \cos \phi)^2 \sin^2 \theta \sin^2 \phi \quad (63)$$

$$A_7 = A_1 - A_2 = (\cos \theta \cos \chi + \sin \theta \sin \chi \cos \phi)^2 - \sin^2 \theta \sin^2 \phi \quad (64)$$

Which in the Mischenko notation is:

$$A_1 = (\cos \beta \sin \theta_o - \sin \beta \cos \theta_o \cos \alpha)^2 \quad (65)$$

$$A_2 = \sin^2 \beta \sin^2 \alpha \quad (66)$$

$$A_3 = A_1^2 = (\cos \beta \sin \theta_o - \sin \beta \cos \theta_o \cos \alpha)^4 \quad (67)$$

$$A_4 = A_2^2 = \sin^4 \beta \sin^4 \alpha \quad (68)$$

$$A_5 = A_1 A_2 = (\cos \beta \sin \theta_o - \sin \beta \cos \theta_o \cos \alpha)^2 \sin^2 \beta \sin^2 \alpha \quad (69)$$

$$A_7 = A_1 - A_2 = (\cos \beta \sin \theta_o - \sin \beta \cos \theta_o \cos \alpha)^2 - \sin^2 \beta \sin^2 \alpha \quad (70)$$

Due to the random orientation this is a random process the mean of which can be computed as:

$$\begin{aligned} \langle Z_h \rangle &= \frac{1}{M} \sum_{i=1}^M \frac{4\lambda^4}{\pi^4} \frac{1}{|K_w|^2} 10^6 \int \left(|f_b(D)|^2 - 2R\{f_b^i(D)(f_b(D) - f_a(D))\} A_{2i} + |f_b(D) - f_a(D)|^2 A_{4i} \right) N(D) dD \\ &= \frac{4\lambda^4}{\pi^4} \frac{1}{|K_w|^2} 10^6 \int \left(|f_b(D)|^2 - 2R\{f_b^i(D)(f_b(D) - f_a(D))\} \langle A_{2i} \rangle + |f_b(D) - f_a(D)|^2 \langle A_{4i} \rangle \right) N(D) dD \end{aligned} \quad (71)$$

Here α has a uniform distribution and β a Gaussian distribution with mean 0° and a certain standard deviation.

The process to compute the simulations is:

1. Compute the forward and backward scattering coefficients $f_{a,b}$

2. Compute the angular moments $\langle A_1 \rangle$ to $\langle A_7 \rangle$
3. Compute the mean polarimetric variables

Chapter 3 **Hydrometeor classification in the literature**

Hydrometeor classification with polarimetric radar is not yet a mature topic and quite some basic research is still necessary. As a result there are multiple approaches in literature and different authors differ in the definition of the hydrometeor types, the classification techniques, etc. Moreover, the classification techniques by different groups are continuously evolving according to the results of new research. Nevertheless we have identified five different groups with operational or semi-operational classification schemes that are well reported in literature and seem to have been widely applied in different institutions.

One of the first classification schemes based on fuzzy logic was developed at Colorado State University and first published by Liu and Chandrasekar (2000) and later improved by Lim et al. (2005). A second scheme, which has been adopted by the American National Weather Service for their WSR-88D network is described in Park et al. (2009). It is based on research performed at NSSL which is synthesized in Straka et al. (2000). This scheme is relevant because the measurement conditions have an impact on the output. Being operational in America, other meteorological services have adopted it.

These first two schemes were largely based on radar observation at S-band and because of that it is not a simple task to extrapolate them to other frequency bands. Other groups have tried to define the membership functions using scattering simulations. Such approach was taken by a group in Aquila University, a first version of their work at C-band is described in Marzano et al. (2007) and later on expanded and performed at X-band in Marzano et al. (2010). Another attempt was performed at X-band by Dolan and Rutledge (2009). However in their version, the membership functions obtained from scattering simulations were modified a-posteriori based on observations. A newer version at C-band is described in Dolan et al. (2013).

All mentioned classification schemes so far have fixed a-priori-defined membership functions. Park et al. (2009) applies weights based on the real-time measurement conditions to modify the output probability but it does not modify the membership functions as such. Al-Sakka et al. (2013) use a different approach. They recognize that the effect of measurement uncertainties is to widen the range of possible values of the polarimetric variables and therefore they try to expand the membership functions according to the measurement conditions.

In the following, more details on the different classification schemes are going to be provided.

3.1 Hydrometeor types

There are multiple approaches to hydrometeor classification. The number of hydrometeor types is not standardized and neither is the underlying assumptions to define each hydrometeor type. As it can be seen in Table 1 practically each author has a different categorization although roughly speaking most of them distinguish between rain, dry snow (aggregates), ice crystals, wet snow, graupel and hail except for Al-Sakka (2013) that does not include the graupel category. So far, no author examines the case of a radar volume containing a mix of species (except for hail mixed with rain).

Table 1 Hydrometeor types according to different authors

Echo Types	Dolan et al. (2013)	Marzano et al. (2010)	Park et al. (2009)	Lim et al. (2005)
Drizzle				
Light Rain				
Moderate Rain				
Heavy Rain				
Ice crystals				
Low Density Graupel				
High Density Graupel/precipitating ice crystals				
Vertically oriented Ice crystals				
Dry Snow (Aggregates)				
Wet Snow				
Large Drops				
Melting Hail				
Hail				
Small hail				
Mixture of Rain+ wet Hail				
Mixture of Rain and Hail				
Large Hail				
Small Rain and Hail				
Large Rain and Hail				
Unknown	X			
Ground Clutter/Anomalous Propagation			X	
Biological Scatters			X	

3.2 Classification techniques

There is also some disagreement on the polarimetric variables used. Most authors use Z_h , Z_{dr} , ρ_{hv} and KDP to construct the membership functions. However some authors do not contemplate all the variables while other add LDR or the texture of reflectivity and differential phase. Some authors use also auxiliary data such as the SNR, the ratio of partial beam blockage or the attenuation to modify the probabilities provided by the membership function. Almost all them use the temperature or the freezing level height and melting layer thickness to refine the classification.

As for the classification technique, most authors use fuzzy logic, except for Marzano et al. (2010). The form of the membership function also varies from author to author. Dolan et al. (2013) and Lim et al.

(2005) use 1-dimensional beta functions whereas Park et al. (2009) uses trapezoidal functions with varying slope. In the case of rain, Park uses 2-dimensional functions. Table 2 summarizes the use of variables in various hydrometeor classification schemes.

Table 2 Use of variables in hydrometeor classification

Variables	Dolan et al. (2013)	Marzano et al. (2010)	Park et al. (2009)	Lim et al. (2005)
Z_h	MF (Beta)	Bayes	MF (Trapezoidal)	MF (Beta)
Z_{dr}	MF	Bayes	MF (2D in rain)	MF
ρ_{hv}	MF		MF /Weight	MF
KDP	MF	Only in Marzano et al. (2008)	MF (2D in rain)	MF
LDR				MF
V_D			Auxiliary	
$SD(Z)$			MF	
$SD(\phi_{dp})$			MF	
T	Multiplicative	Bayes		
SNR			Weight	Aux.
A_h			Weight	
PBB			Weight	
Non uniform beam filling (Vertical and horizontal gradients of $Z_h/Z_{dr}/\phi_{dp}$)			Weight	
Melting layer height and thickness			Multiplicative	Multiplicative

3.3 Assumptions on microphysics

The construction of the membership function also varies from author to author. Most of them largely rely on empirical observations complemented with some degree of modelling. Dolan and Rutledge (2009) and Dolan et al. (2013) (Hereafter jointly referred as Dolan) and Marzano et al. (2007 and 2010) (Hereafter Marzano) are largely relying on modelling, although Dolan refined their classification based on observations. Dolan and Marzano are providing most detail on their assumptions on the classification and therefore they have been used as the main reference, although research from other authors investigating the characteristics of specific hydrometeors have also been used.

3.3.1 Assumptions on individual particles

Table 3 summarizes the assumptions by Dolan and Rutledge (2009) while

Erreur : source de la référence non trouvée summarizes the additional classes in Dolan et al. (2013). In Table 5 the assumptions of Marzano et al. (2007) can be seen whereas in Table 6 the additional classes proposed in Marzano et al. (2010) are also summarized.

Dolan was interested primarily in the expected range of each polarimetric variable for each class so they were only simulating some limit cases. Marzano on the other hand was trying to obtain fully described 2-D membership functions and therefore they performed more simulations.

Table 3 Assumed microphysics of particles by Dolan and Rutledge (2009)

Type	Axis ratio (b/a)	Temp (°C)	Dens (gcm ⁻³)	D _{min} , D _{max} , Δd (mm)
CR	0.125, 0.15, 0.35	-40, -10	0.4, 0.9	0.05, 1.5, 0.005
VI	0.125, 0.15, 0.35	-40, -10	0.4, 0.9	0.05, 1.5, 0.005
AG	0.2, 0.9	-15, 5	0.1, 0.2, BR06, H00	1, 12, 0.1
HDG	0.5, 0.65, 0.75, 0.9, 1.1, 1.25	-5, 5	0.55, 0.65, 0.75, 0.85, 0.9	1, 10, 0.1
LDG	0.5, 0.65, 0.75, 0.9, 1.1, 1.25 0.65, 0.9, 1.1, 1.25	-20, -10 -10	0.25, 0.35, 0.45, 0.55 0.25, 0.35, 0.45, 0.55	1, 10, 0.1 1, 10, 0.1
RAI N	CB90, PP71, J83, BR02, GC84, BC87	3, 10, 20	-	0.5, 10, 0.05
DZ	1.0, 0.9999 GC84	0, 5, 10, 20 5, 20	- -	0.35, 0.55, 0.01 1, 10, 0.05

As it can be seen in the tables, there is little agreement on the range of microphysics. For ice crystals, Dolan allows a smaller axis ratio and smaller size than Marzano, while Marzano considers lower temperature regions as the preferred area of residence. Again, for aggregates, Dolan allows smaller sizes and axis ratio. Marzano allows the presence of aggregates at a much lower temperature than Dolan.

Table 4 Assumed microphysics of particles by Dolan et al (2013)

Type	Axis ratio (b/a)	Temp (°C)	Dens (gcm ⁻³)	Vol. fraction of water in inner sphere	Water coat thickness (mm)	D _{min} , D _{max} , Δd (mm)
VI	0.125, 0.15, 0.35	-40	0.4, 0.9	-	-	0.05, 1.5, 0.005
WS	0.3, 0.5, 0.7	-10, 5	0.2, 0.3	0.3, 0	0.3D	0.5, 12, 0.5
H	0.6, 0.8, 1.1, 1.3	-5	0.7, 0.8, 0.917	0.3, 0.25	0.2, 0.25D	5, 50, 1
LD	0.6, 0.7, 0.8	5, 20	1	-	-	5, 14, 1

Table 5 Assumed microphysics of particles by Marzano et al (2007)

Type	Axis ratio (b/a)	Temp (°C)	Dens (gcm ⁻³)	D _{min} , D _{max} , Δd (mm)
CR	0.5 to 1+rand(0.1)	-72.5 to -5.5	WM	0.2 to 4.8
AG	0.8 to 1+rand(0.1)	-51 to 0	SOMG	1 to 15
WS	0.6 to 1+rand(0.1)	-2.5 to 2.5	LM	1 to 15
G/SH	0.6 to 1+rand(0.1)	-50 to 10	LM	1 to 5
HR	BC	0 to 40	RM	0.6 to 7
MR	BC	0 to 40	RM	0.6 to 7
LR	BC	0 to 40	RM	0.6 to 7
LD	BC	-5 to 35	RM	0.6 to 7
H	0.9 to 1 if D<10 0.6 to 1 if D>10	-20 to 20	WM	5 to 30
H/R	H & HR	H & HR	H & HR	H & HR

Dolan distinguishes between high density and low density Graupel while Marzano has only one Graupel category that is undistinguishable of small hail. The axis ratios in both studies are similar although Dolan allows for prolate spheroids. Dolan also allows for larger sizes. Again Marzano considers a wider temperature span.

Table 6 Assumed microphysics of particles by Marzano et al (2010)

Type	Axis ratio (b/a)	Temp (°C)	Dens (gcm ⁻³)	D _{min} , D _{max} , Δd (mm)
WH	0.8 to 1	-5 to 20	LM	5 to 30
WH/R	50% WH 50% HR			
DR	1	0 to 40	RM	0.1 to 1

Dolan has a single rain category while Marzano distinguishes between heavy rain, moderate rain and light rain. Dolan includes in the simulations several axis ratio models relating axis ratio and drop size while Marzano uses only Beard and Chuang. Dolan allows larger drops than Marzano. Again Marzano has a wider temperature span.

Dolan also has a category drizzle that combines drizzle and light rain. This category is added in Marzano et al. (2010). Marzano allows drizzle droplets up to 1 mm while Dolan reduces it to 0.55 mm. They both assume spherical drops.

Dolan et al. (2013) includes the categories wet snow, hail and large drops/melting hail which are modeled using a two-layer T matrix model. For wet snow, Dolan assumes a lower axis ratio and smaller size than Marzano. Also it allows the presence of wet snow at much lower temperatures (-10°) than Marzano.

For hail, Dolan allows prolate spheroids and much larger sizes (up to 5 cm) than Marzano. It also considers hail to be surrounded by a water coat. Dolan just simulates hail at -5°C while Marzano allows it at temperatures between -20 to 20°C. Marzano distinguishes between hail and wet hail (in their 2010 paper). The axis ratio considered for wet hail is close to one and the drop size is up to 3 cm. Finally, Marzano also considers a mixture of wet hail and rain with 50% probability for each.

As for large drops, Dolan assumes they are oblate with large sizes (up to 14 mm), while Marzano uses a similar parameterization than for rain.

Dolan computes the dielectric factor of solid hydrometeors as a mixture of air and ice using the Maxwell-Garnett mixing formula:

$$|K_s|^2 = \frac{\rho_s}{\rho_i} \left| \frac{\epsilon_r - 1}{\epsilon_r + 2} \right|^2 \quad (72)$$

Where ρ_s is the density of the hydrometeor and ρ_i is the density of pure ice. ϵ_r depends on the temperature and the wavelength. Consequently, the temperature and the density are fundamental parameters for the computation of the scattering matrix. Marzano, does not take into account the difference in ice density for hail and ice crystals and considers only that of pure ice.

As for graupel and wet snow, Marzano uses linear mixing between ice and water of the form:

$$\epsilon_r = M_i \epsilon_{ri} + M_w \epsilon_{rw} \quad (73)$$

With water inclusion varying randomly between 20% to 45% for graupel and 1% to 10% for wet snow. For wet hail, also a linear mixing is used with water inclusion not specified. For aggregates Marzano uses a Maxwell-Garnet mixing dielectric formula as well.

Marzano does not use the two-layer T-matrix model for melting hydrometeors but simple linear mixing relations so it is likely that for these species the results from Dolan are more accurate.

3.3.2 Assumptions on particle size distributions

Table 7 summarizes the assumptions of the first work by Dolan and Table 8 summarizes the expansion. Table 9 summarizes the assumptions in the original work by Marzano and Table 10 summarizes the expansion.

Both authors assume basically a normalized gamma distribution (or inverse exponential when $\mu=0$) as the underlying distribution for all the hydrometeor types except in the case of drizzle for Dolan where a mono-disperse distribution is assumed. For some species, Dolan and Rutledge uses models of the PSD that relate the parameters of the gamma distribution with particle fall rate and explicitly defines those relations while Marzano only mentions that all used relations have been put in terms of the gamma distribution parameters without clearly identifying the source.

Marzano simulates always with a canting angle having the same standard deviation of 5° and mean 0° . Except for hail and ice crystals (where half the simulations are performed at 0° mean and half at 90° mean) and graupel, where it is uniformly distributed between 0° and 180° . Dolan and Rutledge simulates at elevation angles 1° and 30° while Marzano does not explicitly mention them (it is assumed 0°).

Table 7 Assumed microphysics of particle size distributions by Dolan and Rutledge (2009)

Type	$\beta_m(^{\circ})$	$\sigma_{\beta} (^{\circ})$	PSD	D_o (mm)	$N_o(N_w)$ ($\text{mm}^{-1}\text{m}^{-3}$)	μ	Elev ($^{\circ}$)
CR	0	15, 30	Expo	0.18, 0.50, 3.95	189644.0, 21774.1, 287.0	0	1, 30
VI	90	15, 30	Expo	0.18, 0.50, 3.95	189644.0, 21774.1, 287.0	0	1, 30
DS	0	15, 30	Expo	1.02, 3.95	4796.32, 287.0	0	1, 30
HDG	0	10, 20	Expo	3, 4, 5, 5.5, 6.5, 7, 7.5	239.05, 84.13, 37.43, 26.48, 14.44, 11.03, 8.59	0	1, 30
LDG	0 0	10, 20 10, 20	Eq Expo	1.5, 2, 3, 4.5, 5 1.5, 2, 2.5	2959.54, 1041.59, 239.05, 54.86, 37.43 8000	0	1, 30
R	0	1, 4, 10	Gamma	0.5, 1, 1.5, 2, 2.5, 3, 3.5	1e2, 5e2, 1e3, 5e3, 1e4	-0.1, 1, 2, 3, 4	1, 30
DZ	0	1 0.1, 1, 4	Mono Expo	0.1 0.55, 0.77, 0.90, 1.04, 1.09	8000 8000	0 0	1, 30

Table 8 Assumed microphysics of particle size distributions by Dolan et al (2013)

Type	$\beta_m(^{\circ})$	$\sigma_{\beta} (^{\circ})$	PSD	D_o (mm)	$N_o(N_w)$ ($\text{mm}^{-1}\text{m}^{-3}$)	μ	Elev ($^{\circ}$)
VI	90	1, 4	Expo	0.3, 0.6, 0.7	200000, 120000, 4000	0	30
WS	0	45, 60	Expo	0.36, 0.50, 1.02, 2.11	41774.2, 21774.1, 4796.32, 1056.52	0	5
H	0	60, 75, 89, 95	Expo	3, 3.5, 4, 4.5, 5, 7	5000, 400, 300, 200, 100, 80	0	4.3
BD	0	4	Expo	3.5, 4.5, 5.5, 6.5	100, 100, 50, 50	0	1, 5, 15

Table 9 Assumed microphysics of particle size distribution by Marzano et al (2007)

Type	$\beta_m(^{\circ})$	$\sigma_{\beta} (^{\circ})$	PSD	D_o (mm)	$N_o(N_w)$ ($\text{mm}^{-1}\text{m}^{-3}$)	μ	Elev ($^{\circ}$)
CR	0 to 90	5	Expo	1.22 to 3.34	1 to 41	0	
AG	0	5	Expo	0.42 to 1.67	2380 to 42000	0	
WS	0	5	Expo	1.18 to 2.04	1515 to 4800	0	
G/ SH	Unif 0 to 180		Expo	2.29 to 7.34	10 to 270	0	
HR	0	5	Gamma	1.8 to 3.2	2e3 to 9e3	-1 to 4	
MR	0	5	Gamma	1.4 to 2	1e3 to 1e4	-1 to 4	
LR	0	5	Gamma	0.5 to 1.4	1e3 to 2.1e4	-1 to 4	
LD	0	5	Gamma	1.3 to 3.6	15 to 150	-0.94 to 0.87	
H	0 to 90	5	Expo	3.67 to 9.18	100 to 300	0	
H/R	H & HR	H & HR	H & HR	H & HR	H & HR	H & HR	

Table 10 Assumed microphysics of particle size distribution by Marzano et al (2010)

Type	$\beta_m(^{\circ})$	$\sigma_{\beta} (^{\circ})$	PSD	D_o (mm)	$N_o(N_w)$ ($\text{mm}^{-1}\text{m}^{-3}$)	μ	Elev ($^{\circ}$)
WH	0	10	Expo	3.67 to 9.18	100 to 300	0	
WH/R	50% WH 50% HR						
DR	0	5	Gamma	0.36 to 0.49	14000 to 21000	-1 to 4	

Chapter 4 **The MeteoSwiss approach**

The MeteoSwiss approach to hydrometeor classification is based on fuzzy logic. The membership functions are two-dimensional Z_h - Z_{dr} , Z_h - ρ_{hv} and Z_h -KDP and 1-dimensional temperature (obtained from the COSMO-2 numerical weather prediction model). In the inference process the result of each polarimetric variable membership function is additive while the temperature is multiplicative.

It seems clearly unrealistic to attempt a classification based on 10 to 12 hydrometeors using operational radars since due to the uncertainties associated with the polarimetric variables there is a large overlapping between them. Moreover, due to beam broadening, localized phenomena such as hail tends to co-exist with other hydrometeor species.

As a first approach, the species simulated are: rain, aggregates (dry snow), ice crystals, wet snow, and big drops (including hail). Eventually graupel may also be included. A general category precipitation is used when the probabilistic output of the hydrometeor classification is below a certain level of confidence.

The main objective of the classification scheme is to improve precipitation estimation on the ground. By having a bulk identification of the hydrometeors, algorithms tailored specifically to a particular hydrometeor type can be used. For example, since attenuation is hydrometeor-dependent different attenuation corrections can be applied for each hydrometeor type. Likewise, different rainfall rate estimators can be used for each species. Eventually one can imagine an iterative process whereby a first hydrometeor classification with polarimetric variables roughly corrected for attenuation is performed and, after a refined attenuation correction, there is a final classification.

The membership functions are determined using theoretical simulations of the scattering properties of each species by T-matrix calculations (Mischenko, 2000). This approach has the advantage that does not depend on expert observations, there is full control of the input data and it can be computed for different frequencies and different elevation angles. However, the result is limited by the assumptions and the necessary simplifications.

Unlike for other authors (except Al-Sakka 2013), the fuzziness of the membership function is provided by the estimated uncertainty of the measured polarimetric variables. Moreover, weights based on PBB, SNR or attenuation modify to output probability.

In the following chapters, the assumptions over the different simulated species are discussed.

Chapter 5 Simulations of Rain

5.1 Drop shape

The axis ratio of rain droplets have been assumed to be of the form (Thurai et al. 2007):

$$\frac{b}{a} = \begin{cases} 1 & D < 0.7 \text{ mm} \\ 1.173 - 0.5165 D + 0.4698 D^2 - 0.1317 D^3 - 0.0085 D^4 & 0.7 \leq D \leq 1.5 \text{ mm} \\ 1.065 - 0.0625 D - 0.00399 D^2 + 0.000766 D^3 - 0.00004095 D^4 & D > 1.5 \text{ mm} \end{cases} \quad (74)$$

Drops as large as 7 mm will be used in the simulations. According to Huang et al. 2013 drops fall with a canting angle between of 4° and 7° but we have assumed a canting angle of 10°.

5.2 Drop Size Distribution

Rain is typically assumed to have a gamma drop size distribution of the form:

$$N(D) = N_o D^\mu e^{-\Lambda D} \left[\frac{1}{m^3 \text{ mm}} \right] \quad (75)$$

Or, written in normalized form:

$$N(D) = N_w f(\mu) \left(\frac{D}{D_o} \right)^\mu e^{-\Lambda D} \quad (76)$$

With:

$$f(\mu) = \frac{6}{3.67^4} \frac{(3.67 + \mu)^{\mu+4}}{\Gamma(\mu+4)} \quad (77)$$

Where:

$$\Lambda = \frac{3.67 + \mu}{D_o} [mm^{-1}] \quad (78)$$

If the distribution extends to infinite sizes (or very large). D_o is the median equivalent volume diameter. D is the equivalent volume diameter (the diameter if the droplet was an sphere of equivalent volume).

And

$$N_o = N_w f(\mu) D_o^{-\mu} \left[\frac{1}{m^3} \frac{1}{mm^{\mu+1}} \right] \quad (79)$$

The gamma drop size distribution is characterized by D_o , N_w and μ :

$$D_o = \frac{3.67 + \mu}{\Lambda} [mm] \quad (80)$$

$$N_w = \frac{N_o}{f(\mu) D_o^{-\mu}} \left[\frac{1}{m^3} \frac{1}{mm} \right] \quad (81)$$

If $\mu=0$ then the gamma distribution reduces to an exponential distribution and $N_w=N_o$.

The range of the parameters of the gamma distribution are typically obtained from disdrometer data by fitting a gamma distribution. The disdrometer data is sampled over a time period (typically 1 min). Although gamma distributions are widely used and there is evidence that in the long term rainfall does have a gamma distribution (Leinonen et al. 2012) radar measurements are instantaneous and sampling a limited volume. Consequently, the underlying DSD of radar measurements may not always be adequately represented by a gamma distribution (Ignaccolo and De Michele, 2014). For this reason we have decided not to fit any distribution but to use PARSIVEL disdrometer data as it is.

We use data from an experiment performed by EPFL during approximately 15 months. During this experiment a set of 16 PARSIVEL disdrometers were installed in a grid of approximately 1 km² (Jaffrain and Berne, 2011). Filtered data is provided with a sample resolution of 1 min. If data from each single disdrometer were used individually, we would suffer from a representativeness error since disdrometers are point measurement instruments while radar data is volumetric (Jaffrain and Berne, 2012). To minimize the representativeness error we combine the measurements of all 16 disdrometers by averaging the detected number of droplets in each bin. We select measurements where all the disdrometers were measuring rain.

It should be noticed that the use of disdrometer data is also subject to a certain degree of error: In the first place, although theoretically the PARSIVEL disdrometers cover a range from 0 to 26 mm in practice no drops are detectable for the first two classes so the minimum detectable droplet has a diameter of approx. 0.3 mm and therefore the population of small drops is underrepresented. In the second place the width of the bin for large drops is rather large (1 mm) so a quantization error may be present, particularly at dimensions where there are resonant effects.

Another source of uncertainty concerning the membership functions is whether 15 months of data in Lausanne suffice to have a representative climatology of rainfall DSD in Switzerland.

5.3 Liquid water content

To compute the liquid water content we have to take into account that the volume of a sphere is:

$$V = \frac{4}{3} \pi r^3 = \frac{\pi}{6} D^3 \quad (82)$$

Therefore:

$$l_{wc} = \frac{\pi}{6} \int D^3 N(D) dD \left[\frac{mm^3}{m^3} \right] \quad (83)$$

If we want to express the liquid water content in terms of mass of water we have:

$$lwc_m = \rho_w lwc_v \left[\frac{g}{m^3} \right] \quad (84)$$

Where ρ_w is the density of water, i.e: 0.0009999720 g/mm³ at normal pressure and 4°C.

5.4 Rainfall rate

The rainfall rate is related to the fall velocity of the droplets as:

$$R = 0.6\pi 10^{-3} \int v(D) D^3 N(D) dD \left[\frac{mm}{h} \right] \quad (85)$$

Where the fall velocity of the droplets can be parameterized as:

$$v(D) = 3.78 D^{0.67} \left(\frac{\rho_o}{\rho} \right)^{0.375+0.025D} \left[\frac{m}{s} \right] \quad (86)$$

Where $\rho_o=1.22$ is the air density at sea level (assuming standard atmosphere) and ρ is the air density at altitude in Kg/m³.

5.5 Refractive index

To compute the scattering properties of rain we have to know the refractive index of water. The refractive index of water for frequencies between 0 and 1000 GHz, temperatures from 0°C to 30°C and salinities from 0 to 40 promille are according to the chapter by Ellison in the book by Matzler (2006):

$$\varepsilon_r = \frac{\delta_1}{1 - j \frac{2\pi}{1000} f \tau_1} + \frac{\delta_2}{1 - j \frac{2\pi}{1000} f \tau_2} + \varepsilon_{inf} + j 17.9751 \frac{\sigma}{f} \quad (87)$$

$$\delta_1 = \varepsilon_s - \varepsilon_1 \quad (88)$$

$$\delta_2 = \varepsilon_1 - \varepsilon_{inf} \quad (89)$$

$$\tau_1 = (0.17667420 - 0.20491560 \cdot 10^{-3} S) e^{\frac{0.58366888 \cdot 10^3}{T+0.12634992 \cdot 10^3}} \quad (90)$$

$$\tau_2 = (0.69227972 \cdot 10^{-1} + 0.38957681 \cdot 10^{-3} S) e^{\frac{0.30742330 \cdot 10^3}{T+0.12634992 \cdot 10^3}} \quad (91)$$

$$\varepsilon_{inf} = 0.37245044 \cdot 10^1 + 0.92609781 \cdot 10^{-2} T - 0.26093754 \cdot 10^{-1} S \quad (92)$$

$$\varepsilon_1 = 0.63000075 \cdot 10^1 e^{0.26242021 \cdot 10^{-2} T + 0.42984155 \cdot 10^{-2} S - 0.34414591 \cdot 10^{-4} ST} \quad (93)$$

$$\varepsilon_s = 87.85306 e^{-0.00456992 T - 0.46606917 \cdot 10^{-2} S + 0.2608787 \cdot 10^{-4} S^2 + 0.63926782 \cdot 10^{-5} ST} \quad (94)$$

$$\sigma = \sigma_{35} \cdot RTQ \cdot R15 \quad (95)$$

$$\sigma_{35} = 2.903602 + 8.607 \cdot 10^{-2} T + 4.73881 \cdot 10^{-4} T^2 - 2.991 \cdot 10^{-6} T^3 + 4.3041 \cdot 10^{-9} T^4 \quad (96)$$

$$R_{15} = S \frac{37.5109 + 5.45216 S + 1.449 \cdot 10^{-2} S^2}{1004.75 + 182.283 S + S^2} \quad (97)$$

$$RTQ = 1 + \alpha_o \frac{T - 15}{\alpha_1 + T} \quad (98)$$

$$\alpha_o = \frac{6.9431 + 3.2841 S - 0.0099486 S^2}{84.850 + 69.204 S + S^2} \quad (99)$$

$$\alpha_1 = 49.843 - 0.2276 S + 0.00198 S^2 \quad (100)$$

Where T is the temperature in °C and f is the frequency in GHz.

Chapter 6 Simulation of ice crystals

6.1 Particle shape

Ice crystals, i.e. particles that grow by deposition (diffusion of water vapor) are difficult to simulate in the first place due to the large variability of shapes and densities co-existing. However, it has been shown that the particle formation is strongly dependent on temperature and water saturation (Pruppacher and Klett, 1997). In general terms, it can be distinguished between plate-like and column-like crystals. Plate-like crystals preferably grow along the basal plane while column-like crystals grow along the axis of symmetry. The most updated laboratory experiments from Bailey and Hallet (2009) have revealed that at temperatures between 0 and -4 °C, plates are prevalent. From -4 to -8 °C needles and hollow columns are more abundant. Between -8 and -22 there is a prevalence of plates and dendrites. At lower temperature there is a polycrystalline regime with plate-like particles prevalent down to -40°C and column-like further down. Fig. 3 summarizes the type of ice particles according to temperature and supersaturation.

Although ice crystals may be created and exist at any altitude above the iso-0°C, in practice they are only prevalent at the top level of the clouds. At lower levels, where more particles are formed, the prevailing growing mechanism is collision. Collisions of ice crystals with other ice crystals form aggregates while collisions of ice crystals with supercooled water form graupel and, eventually, hail.

Table 11 Coefficients of the minor-major dimension relationship

Type	a	b	D _{max} [mm]
P1e Dendrite	0.0418	0.377	0.6-5.3
C1g Solid thick plate	0.23	0.778	0.01-1
P1a Hexagonal plate	0.0473	0.474	0.01-3
C1e Solid column	0.637 D/h<2 0.308 D/h>2	0.958 0.927	0.01-1
C1f Hollow column	0.541 D/h<2 0.309 D/h>2	0.892 0.930	0.01-1 0.01-1
N1e Long solid column	0.129	0.437	0.2-1.5
C1c Solid bullet	0.250	0.786	<0.3
C1d Hollow bullet	0.185	0.532	>0.3
N1a Elementary needle	0.075	0.611	0.6-2.7

The aspect ratio of ice crystals is size dependent and empirical relations of the form:

$$h = a D_{max}^b \quad (101)$$

where h is the smallest dimension of the ice crystal (the thickness in the case of plates and the width in the case of columns) and D_{\max} is the largest one (diameter in the case of plates and length in the case of columns) have been derived. Parameters from Matrosov et al. (1996) and Pruppacher and Klett (1997) are summarized in Table 11.

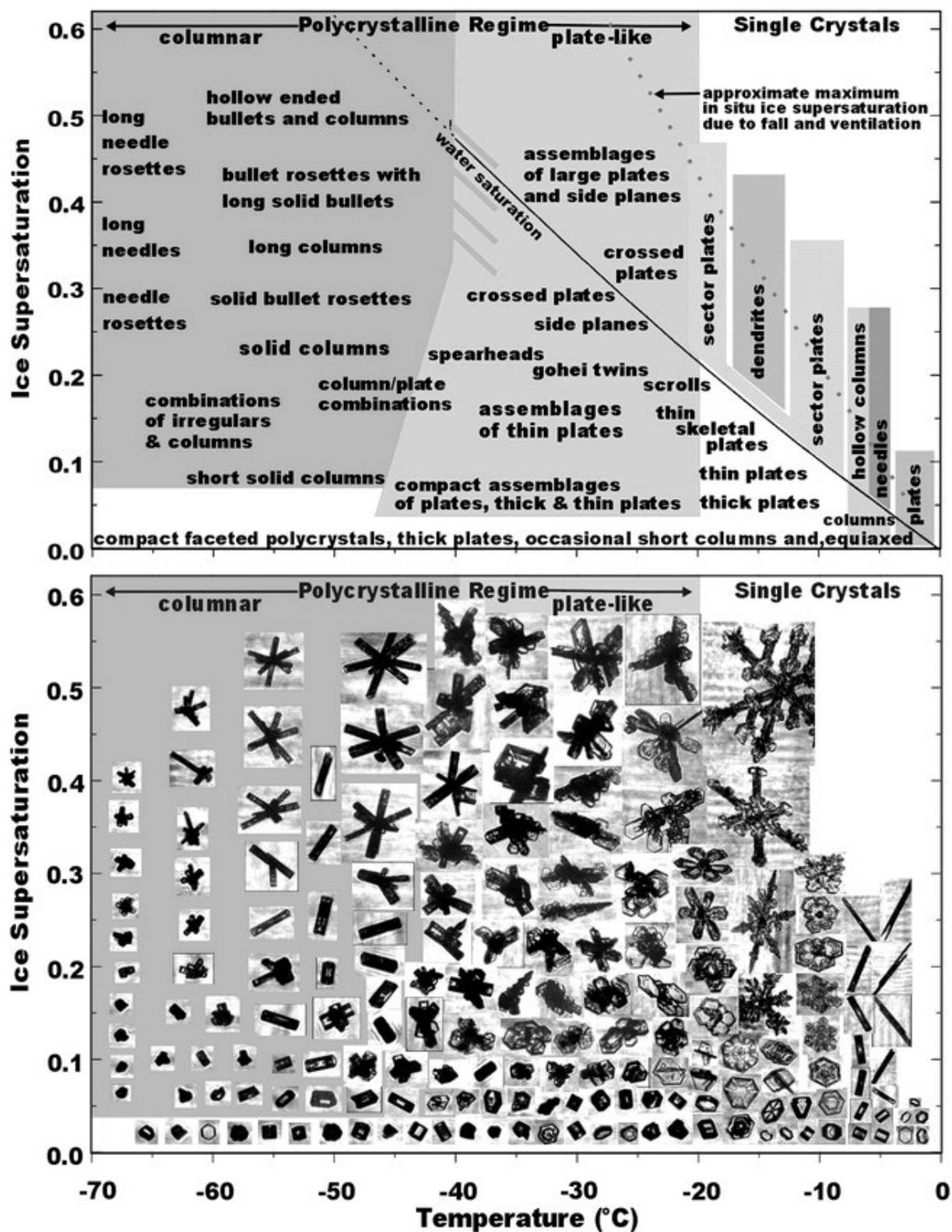


Fig. 3 Distribution of ice particles as a function of temperature and supersaturation

We will focus on the lower cloud layer (temperatures up to -30°C) and assume a similar simplified model similar to that of Andric et al (2013) with small (up to 0.3 mm) near-spherical crystals with high density predominant at -30°C . Solid thick plates (up to 1 mm) at -20°C and dendrites (up to 3 mm) at -15°C . It is assumed that further down the cloud aggregates are predominant. We will approximate all the particles by oblate spheroids with the major axis equal to the major dimension and the minor axis equal to the thickness. It should be noticed that due to computation stability issues the minimum axis ratio that can be simulated is 0.15.

6.2 Particle size distribution

Heymsfield et al (2013) collected a large dataset of in situ observations in ice clouds. In their data they show that the particle size distribution of ice crystals can be reasonably approximated by an exponential and they provide fitted relationships between N_t (total number concentration) and Λ as a function of temperature. They find that at temperatures above -60°C the total ice number concentrations can be approximated as:

$$N_t = \begin{cases} 9.7 \cdot 10^3 e^{-0.026 T} & \text{stratiform} \\ 3.1 \cdot 10^3 e^{-0.049 T} & \text{convective} \end{cases} \left[\frac{1}{m^3} \right] \quad (102)$$

And the slope parameter as:

$$\Lambda = \begin{cases} 1.53 e^{-0.053 T} & \text{stratiform} \\ 0.34 e^{-0.083 T} & \text{convective} \end{cases} \left[\frac{1}{mm} \right] \quad (103)$$

We assume that for each temperature the values of N_t and Λ are constrained between the convective and the stratiform cases. Therefore we first obtain the range of Λ and then we obtain N_o from N_t as:

$$N_t = \int_{D_{min}}^{D_{max}} N(D) dD = \int_{D_{min}}^{D_{max}} N_o e^{-\Lambda D} dD \quad (104)$$

$$N_o = \frac{N_t}{\int_{D_{min}}^{D_{max}} e^{-\Lambda D} dD} \quad (105)$$

The simulation is based on Dolan and Rutledge (2009). An exponential particle size distribution based on Sekhon and Srivastava (1970) is assumed where Delta and N_o are related to equivalent snowfall rate as:

$$\Lambda = 2.29 R^{-0.45} \left[\frac{1}{mm} \right] \quad (106)$$

And:

$$N_o = 2500 R^{-0.94} \left[\frac{1}{m^3} \frac{1}{mm} \right] \quad (107)$$

The equivalent volume diameter was considered small: up to 1.5 mm. Because of the limit in size of the particles the relation between D_o and Δ in this case is:

$$D_o = \frac{3.2}{\Delta} [mm] \quad (108)$$

It should be noticed that the particle size distribution is a function of the equivalent volume diameter while most relations for ice crystals are depending on the larger dimension. Assuming the particle to be approximated by an spheroid with minor semiaxis b and major semiaxis $a = D_{max}/2$ and axis ratio $AR = b/a$ we can obtain the following relation:

$$V = \frac{4}{3} \pi a^2 b = \frac{4}{3} \pi a^3 AR = \frac{\pi}{6} D^3 \quad (109)$$

$$D = D_{max} \sqrt[3]{AR} \quad (110)$$

6.3 Equivalent liquid water content

To compute the equivalent liquid water content we have first to relate the mass of the particle with the density of water, it is assumed that the air component has negligible mass:

$$lwc_e = \frac{1}{\rho_w} \int m(D) N(D) dD \left[\frac{mm^3}{m^3} \right] \quad (111)$$

With ρ_w the water density at 4°C, i.e 0.0009999720 [g/mm³].

The density of ice crystals tend to vary with size. In general terms, smaller particles have a density close to true ice while the density of larger particles decreases rapidly with size. Empirical relations between mass and the largest dimension of the type:

$$m = c D_{max}^d \quad (112)$$

Where the mass is in g and the largest dimension in mm have been derived. Table 12 summarizes some of the coefficients found in Pruppacher and Klett (1997).

Table 12 Coefficients of the mass-major dimension relation

Type	c	d	D _{max} [mm]
P1e Dendrite	3.14e-6	2.29	0.6-5.3
C1g Solid thick plate	-	-	-
P1a Hexagonal plate	1.84e-5	3.31	0.01-3
C1e Solid column	6.4e-5	2.6	0.01-1
C1f Hollow column	3.7e-5	1.8	0.01-1
N1e Long solid column	1.2e-5	1.8	0.2-1.5
C1c Solid bullet	-	-	-
C1d Hollow bullet	-	-	-
N1a Elementary needle	4.9e-6	1.8	0.6-2.7

6.4 Equivalent rainfall rate

The equivalent rainfall rate (melted liquid) is related to the velocity as:

$$R_e = \frac{3.6}{1000} \frac{1}{\rho_w} \int m(D) v(D) N(D) dD \left[\frac{mm}{h} \right] \quad (113)$$

Heymsfield and Westbrook (2010) have developed an analytical formula that relates the terminal velocity v_t of ice particles to their mass and projected area:

$$v_t = \frac{\eta Re}{\rho_a D_{max}} \quad (114)$$

Where Re is the Reynolds number given by:

$$\Re = \frac{\delta_0^2}{4} \left(\sqrt{1 + \frac{4 \sqrt{X^i}}{\delta_0^2 \sqrt{C_o}}} - 1 \right)^2 \quad (115)$$

With $C_o=0.35$ and $\delta_o=8.0$. And:

$$X^i = \frac{\rho_a}{\eta^2} \frac{8mg}{\pi A_r^{0.5}} \quad (116)$$

Where m is the particle mass that can be expressed as in (60). A_r is the area ratio, the ratio of the particle's projected area A to the area of a circumscribing circle:

$$A_r = \frac{A}{\frac{\pi}{4} D_{max}^2} \quad (117)$$

Aspect ratios for various shapes can be found in Table 13. g is the standard gravity 9.80665 m/s^2 , ρ_a is the air density (1.22 Kg/m^3 at sea level) and η is the air viscosity ($1.81 \cdot 10^{-5} \text{ Kg/(m s)}$ at 15°C and standard atmosphere).

Table 13 Area ratio of various shapes

Type	A_r
Hexagonal plate	0.83
Broad Branched crystals	0.74
Thin circular disks	1
Stellar crystal	0.185
Dendrites	0.28
Stellar with end plates	0.47
Aggregate (star shape)	0.55
Aggregate (H shape)	0.39
Aggregate (Cross shape)	0.28
Aggregate (linear chain)	0.14
Graupel	0.8
Sphere	1

6.5 Refractive index

Ice crystals can be seen as a mixed of pure ice and air. Using the Maxwell-Garnett formula the dielectric factor of ice crystals can be expressed in terms of the dielectric factor of pure ice and their density:

$$|K_s|^2 = \left| \frac{\rho_s \varepsilon_r - 1}{\rho_i \varepsilon_r + 2} \right|^2 \quad (118)$$

Where ρ_i is density of pure ice and ε_r is the dielectric constant of pure ice. Here the assumption is that spherical ice inclusions (modelled as identical discrete spheres uniformly distributed) are embedded in an air matrix. The dielectric constant of pure ice is computed as (Matzler, 2006):

$$\varepsilon_1 = 3.1884 + 9.1 \cdot 10^{-4} (T - 273.15) \quad (119)$$

$$\varepsilon_2 = \frac{\alpha}{f} + \beta f \quad (120)$$

$$\alpha = (0.00504 + 0.0062 \theta) e^{-22.1\theta} \quad (121)$$

$$\beta = \frac{0.0207 e^{\frac{335}{T}}}{(T) \left(e^{\frac{335}{T}} - 1 \right)^2} + 1.16 \cdot 10^{-11} f^2 + e^{-9.963 + 0.0372(T - 273.16)} \quad (122)$$

$$\theta = \frac{300}{T} - 1 \quad (123)$$

Where T is temperature in Kelvin and f is frequency in GHz.

ρ_s is the density of the ice crystal, which has been empirically related to its largest dimension as:

$$\rho = e D^f \quad (124)$$

Where the density is in g/mm³. Coefficients c and d for some selected ice crystals can be seen in Table 14 (Pruppacher and Klett 1997).

Table 14 Coefficients of the density-major dimension relation

Type	e	f	D [mm]
P1e Dendrite	0.000588	-0.377	>0.3
C1g Solid thick plate	0.000916	0	-
P1a Hexagonal plate	0.000916	0	-
C1e Solid column	0.000916	0	-
C1f Hollow column	0.00065 0.000848	-0.0915 (cold region) -0.014 (warm region)	>0.028 >0.014
N1e Long solid column	0.000916	0.	-
C1c Solid bullet	0.000916	0.	-
C1d Hollow bullet	0.00078	-0.0038	>0.1
N1a Elementary needle	0.000916	0.	-

Chapter 7 Simulations of aggregates (Dry Snow)

7.1 Particle shape

What we mean here for aggregates are particles formed by the aggregation by collision of individual ice crystals. According to Matrosov et al (2009), aggregates can be approximate by oblate spheroids with axis ratios between 0.6 and 0.8. However Brandes et al (2007) made measurements on the ground and they found that on average the axis ratio is very close to 1 albeit with significant scattering. We have simulated an axis ratio of 0.8. According to Ryzhkov et al (2011) the canting angle of aggregates has a standard deviation of 40° because they tumble with the winds.

7.2 Particle Size Distribution

Brandes et al (2007) show that dry snow precipitation can be well characterized by an exponential particle size distribution, i.e $\mu=0$. According to their dataset (See Fig. 4) and focusing in the temperatures between around -2° , which are the most likely to contain mostly aggregates Λ varies between 1 and 6 mm^{-1} and N_0 from 1000 to 30000 $\text{mm}^{-1}\text{m}^{-3}$, consequently D_0 ranges from 0.61 to 3.67 mm and $N_w=N_0$.

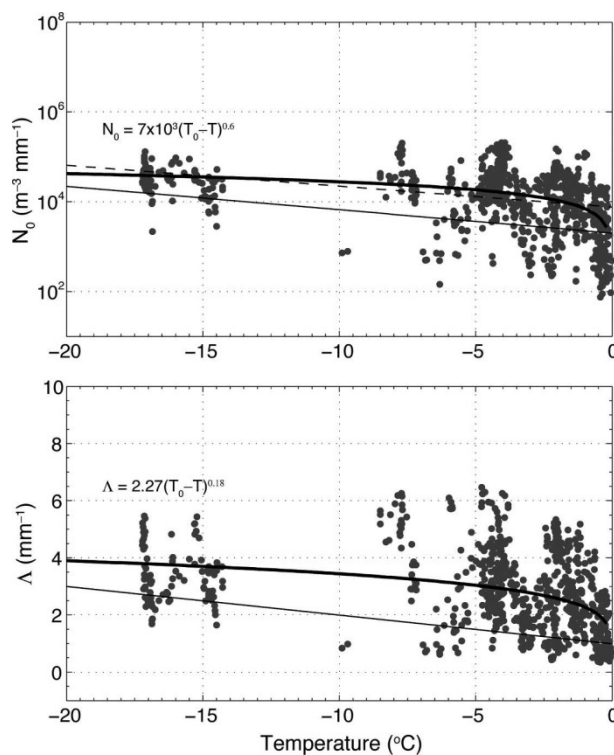


Fig. 4 Concentration and slope parameters for truncated exponential PSDs plotted against surface air temperature.

7.3 Equivalent liquid water content

In our simulations we have assumed the following relation between dimension and mass from Matrosov et al (2009):

$$m(D) = \begin{cases} 0.00003 D^2 & D < 2 \text{ mm} \\ 0.000211873 D^{2.5} & D \geq 2 \text{ mm} \end{cases} [g] \quad (125)$$

And the equivalent liquid water content can be computed as in section 6.3.

7.4 Equivalent rainfall rate

According to the approximation by Matrosov (2007):

$$v(D) = \begin{cases} 0.3 + 0.5 (\log(D) + 1) & 0.1 < D < 10 \text{ mm} \\ 1.3 & D \geq 10 \text{ mm} \end{cases} \left[\frac{m}{s} \right] \quad (126)$$

And the rainfall rate can be computed as in section 6.4.

7.5 Refractive index

The refractive index of aggregates can be computed as in section 6.5. Considering that the aggregate can be well approximated by an spheroid, its density will be given by:

$$\rho_s = \frac{m(D)}{\frac{\pi}{6} D^3} \quad (127)$$

There exist other more complex scattering models for snowflakes such as the one that is going to be used for wet snow where a distinction between a higher density inner core and a lower density shell is made. However the differences in case of dry snow, as shown by Fabry and Szyrmer (1999) are not that significant.

Chapter 8 Simulations of wet snow

8.1 Particle shape

The axis ratio of wet snow will progressively change from that of dry snow to that of a water droplet:

$$r_{ws} = r_{ds} + f_{mw}(r_w - r_{ds}) \quad (128)$$

Where f_{mw} is the mass water fraction (Ryzhkov et al. 2011).

According to Fabry and Szyrmer (1999) the best model characterizing dry snow aggregates is composed of two layers. The inner layer has a higher density of ice, while the outer layer has a much lower density. Consequently the inner layer can be characterized as air inclusions in an ice matrix while the outer layer is characterized as ice inclusions in an air matrix. When the snowflake is significantly melted the inner core will be soaked by water filling the space between the remaining ice with some air cavities still present. Therefore it can be characterized as a matrix of ice inclusions in water that has air inclusions. In the outer, less dense layer, air is predominant and therefore it can be characterized as an inclusion of ice in a water matrix in an air matrix. The mass water fraction will increase with the rate of melting until eventually become 1.

8.2 Particle size distribution

The initial particle size distribution is the same as for dry aggregates. By conservation of the mass the number concentration of droplets remain the same during the melting process. However, because the equivalent diameter of the particle varies during melting, the size of the bins and the shape of the PSD will vary.

8.3 Equivalent liquid water content

The equivalent liquid water content is the same as for dry snow.

8.4 Equivalent rainfall rate

The equivalent rainfall rate will have a transition from that of dry snow to that of rain according to the mass water fraction. We will use the same approach as Szyrmer and Zawadzki (1999). In their approach they relate the fall velocity of the melting snow to that of the equivalent rain drop as:

$$v_m(D_w, f_{mw}) \approx \frac{1}{g(f_{mw})} v_r(D_w) \quad (129)$$

With:

$$g(f_{mw}) = \frac{V_r(D_w)}{V_m(D_w, f_{mw})} \approx \frac{V_r(D_w)}{V_s(D_w)} - C_g f_{mw} - C_g f_{mw}^2 \quad (130)$$

Where:

$$C_g = 0.5 \left(\frac{V_r(D_w)}{V_s(D_w)} - 1 \right) \quad (131)$$

Which approximates the empirical results by Mitra et al (1990). Here v_r has the form:

$$v_r(D_w) = a D_w^b \quad (132)$$

Whereas the velocity of dry snow has the form:

$$v_s(D_w) = \alpha D_w^\beta \quad (133)$$

Szyrmer and Zawadzki use (1999) use $a=4.245$ and $b=0.6$, which is slightly different from what we use for rain: $a=3.78$ and $b=0.67$. For consistency we will use our own a . α and β are taken as 0.898 and 0.61 respectively with the authors specifying that they refer to a mixture of dendrites and aggregates of plates. Note that the above simplification is only valid if b and β are similar.

8.5 Mass water fraction

According to Mitra et al. (1990) the rate of heat arriving at a snowflake that has begun to melt varies according to:

$$\frac{dq}{dt} = -L_m \frac{dm_i}{dt} - L_v \frac{dm_w}{dt} \quad (134)$$

Where $\frac{dm_i}{dt}$ is the rate at which ice melts, $\frac{dm_w}{dt}$ is the rate at which melt water is evaporated L_m and L_v are the enthalpy of melting and vaporization, respectively which can be written as:

$$L_m = 3.335e5 \left(1 + 0.006(T - T_0) - 3.14e-5(T - T_0)^2 \right) \left[\frac{J}{Kg} \right] \quad (135)$$

$$L_v = 2.499e6 \left(\frac{T_0}{T} \right)^{0.167 + 3.67e-4 T} \left[\frac{J}{Kg} \right] \quad (136)$$

For a snowflake is considered $T=0^\circ\text{C}$. The rate at which the ice melts can be found to be:

$$\frac{-dm_i}{dt} = \frac{4\pi\bar{f}C_{ms}}{L_m} \left(k_a(T_\infty(t) - T_0) + \frac{D_v M_w L_v}{R} \left(\frac{\frac{RH}{100} e_{sat,w}(T_\infty(t))}{T_\infty(t)} - \frac{e_{sat,w}(T_0)}{T_0} \right) \right) \left[\frac{Kg}{s} \right] \quad (137)$$

Here $e_{sat,w}(T_\infty(t))$ is the saturation vapor pressure in the environment, which can be written as (Alduchov and Eskridge, 1996):

$$e_{sat,w}(T) = 6.1094 \cdot 10^2 e^{\frac{17.625 T}{243.04 + T}} \left[Pa = \frac{Kg}{m \cdot s^2} \right] \quad (138)$$

D_v is the diffusivity of water vapor in air expressed as:

$$D_v = 2.11e-5 \left(\frac{T}{T_0} \right) \left(\frac{p_0}{p} \right) \left[\frac{m^2}{s} \right] \quad (139)$$

Where $p_0 = 100$ Pa is the air pressure at the surface and p is the air pressure. This expression is evaluated at $T = 0^\circ C$ for snowflakes.

$M_w = 0.018 \frac{Kg}{mol}$ is the molecular weight of water. $R = 8.314 \frac{J}{mol \cdot K}$ is the ideal gas constant.

$T_0 = 273.15$ K, $T_\infty(t)$ is the temperature of the air varying with time, RH is the relative humidity of the air around the melting flake and k_a is the thermal conductivity of air (with $T_\infty = 0^\circ C$):

$$k_a = (2.381 + 0.0071(T_\infty - T_0)) 10^{-2} \left[\frac{J}{m \cdot s \cdot K} \right] \quad (140)$$

\bar{f} is the ventilation coefficient for heat and vapor transfer (assuming that they are similar). The ventilation coefficient for a snowflake can be written as:

$$\bar{f} = \begin{cases} 1 + 0.14 \chi^2 & \chi \leq 1.0 \\ 0.86 + 0.28 \chi & \chi > 1.0 \end{cases} \quad (141)$$

With:

$$\chi = N_{Sch,v}^{1/3} N_{\mathcal{R},L}^{1/2} \quad (142)$$

Where the Schmidt number is written as:

$$N_{Sc,v} = \frac{\nu_a}{D_v} \quad (143)$$

Where ν_a is the kinematic viscosity of air given by:

$$\nu_a = \frac{\eta}{\rho_a} \quad (144)$$

With $\eta = 1.81 \cdot 10^{-5} \frac{Kg}{m \cdot s}$ the dynamic viscosity of air and $\rho_a = 1.22 \frac{Kg}{m^3}$ the air density.

The Reynolds number is computed as:

$$N_{\mathcal{R},L} = \frac{L_{ms} \dot{v}_{ms}}{\nu_a} \quad (145)$$

v_{ms} is the fall speed of the melting snowflake. And L_{ms}^* is the length parameter of the melting flake given by:

$$L_{ms}^* = \frac{\Omega_{ms}}{P_{ms}} \quad (146)$$

Where P_{ms} is the perimeter:

$$P_{ms} = \pi D_{ms} \quad (147)$$

And Ω_{ms} is the surface area given by:

$$\Omega_{ms} = \pi \left(\frac{D_{ms}}{2} \right)^2 \left(2 + \pi (AR)_{ms} \frac{1}{\epsilon} \ln \frac{1+\epsilon}{1-\epsilon} \right) \quad (148)$$

$$\epsilon = \sqrt{1 - (AR)_{ms}^2} \quad (149)$$

$(AR)_{ms}$ is the axis ratio of the melting flake.

C_{ms} is the capacitance of the melting snowflake which can be written as:

$$C_{ms} = \gamma C_{s,0} \quad (150)$$

$$C_{s,0} = \frac{D_{ms} \epsilon}{2 \sin^{-1} \epsilon} \quad (151)$$

And γ varying linearly with mass water fraction from 0.8 for a dry snowflake to 1 for a completely melted snowflake, i.e.:

$$\gamma = 0.8 + 0.2 f_{mw} \quad (152)$$

Instead of as function of time the melting can be expressed as function of distance from the iso-0° using the velocity:

$$\frac{d m_i}{d h} = \frac{1}{v_{ms}(t)} \frac{d m_i}{d t} \quad (153)$$

By conservation of the mass the lost ice mass is transformed into water mass:

$$\frac{d m_w}{d h} = \frac{-d m_i}{d h} \quad (154)$$

And the fraction mass water considering a snowflake of initial mass m at a given altitude is the integral:

$$f_{mw} = \frac{1}{m} \int_{h=h_{iso0^\circ}-h'}^{h=h_{iso0^\circ}} \frac{d m_w}{d h} d h \quad (155)$$

8.6 Refractive index

According to Szyrmer and Fabry (1999) the average dielectric constant of a body composed of randomly oriented elliptical inclusions in another medium can be computed as:

$$\epsilon_{av} = \frac{(1-f_{vi})\epsilon_m + f_{vi}\beta\epsilon_i}{1-f_{vi}+f_{vi}\beta} \quad (156)$$

With:

$$\beta = \frac{2\epsilon_m}{\epsilon_i - \epsilon_m} \left(\frac{\epsilon_i}{\epsilon_i - \epsilon_m} \ln \left(\frac{\epsilon_i}{\epsilon_m} \right) - 1 \right) \quad (157)$$

Where ϵ_m is the dielectric constant of the matrix, ϵ_i is the dielectric constant of the inclusions and f_{vi} is the volume fraction of the inclusions.

In dry snow the inner core is computed as inclusions of air in an ice matrix while the outer core is computed as inclusions of ice in an air matrix. When the snowflakes are significantly melted the inner core is treated as air inclusions in a (ice inclusions in a water matrix) matrix while the outer core is treated as (ice inclusions in a water matrix) inclusions in an air matrix.

Since during the process of melting the outer layer melts faster, the relative position of the size of the core respect to the total snowflake size varies with the fraction of water. Supposing a snow flake of diameter D_s , where the density transition occurs at αD_s the total snow density can be expressed as:

$$\rho_s D_s^3 = \rho_{sin} (\alpha D_s)^3 + \rho_{sout} (D_s^3 - (\alpha D_s)^3) \quad (158)$$

Where ρ_{sin} is the snow density in the core of the snowflake and ρ_{sout} is the snow density in the outer layer. The average density of a snow flake varies as:

$$\rho_s = c D_s^d \quad (159)$$

Consequently the density of the inner core has to be equal to that of a snowflake that has the same size as the inner core:

$$\rho_{sin} = \rho_s \alpha^d \quad (160)$$

Combining Eq. 126 and Eq. 124:

$$\rho_{sout} = \rho_s \frac{1 - \alpha^{3+d}}{1 - \alpha^3} \quad (161)$$

Here α is set arbitrarily as 0.5 whereas d is typically -1 for aggregates.

Now, the density of the melting snowflake can be written as:

$$\rho_m = \frac{\rho_s \rho_w}{f_{mw} \rho_s + (1 - f_{mw}) \rho_w} \quad (162)$$

The density in the inner core and the outer shell can also be computed with the same formula:

$$\rho_{min} = \frac{\rho_{sin} \rho_w}{f_{mw} \rho_{sin} + (1 - f_{mw}) \rho_w} \quad (163)$$

$$\rho_{mout} = \frac{\rho_{sout} \rho_w}{f_{mw} \rho_{sout} + (1 - f_{mw}) \rho_w} \quad (164)$$

Using Eq. 156 but for melting snowflakes we can obtain the relative position of the transition from the inner to the outer core:

$$\alpha_m = \left(\frac{\rho_m D_m^3 - \rho_{mout} D_m^3}{\rho_{min} D_m^3 - \rho_{mout} D_m^3} \right)^{1/3} \quad (165)$$

Whereas, by conservation of the mass:

$$\rho_s D_s^3 = \rho_m D_m^3 \quad (166)$$

Consequently, assuming the volume water fraction is the same for the inner core and the outer shell, the density of the melting snowflake can be derived from Eq. 128. The diameter of the melting snowflake can be computed from Eq. 132. Finally, Eq. 131 provides the relative position of the transition between the inner core and the outer shell.

Chapter 9 Simulations of hail/melting hail

9.1 Particle shape

Hail is formed in convective situations where a large updraft causes drops to be lifted above the melting layer. If the speed of the drop is large enough they have no time to freeze and remain as supercooled water drops. Ice crystals in those levels may grow by riming of this supercool water.

Hail is a particularly complex phenomenon to simulate because its scattering properties are widely variable. Theoretically dry hail has an axis ratio close to 1 and size from 0.5 cm up to 5 cm, although giant hail larger than 5 cm have been observed. It also has a wide canting angle as it falls tumbling due to the large wind shear. Ryzhkov et al. (2011) assumes the following axis ratio:

$$r_{dh} = \begin{cases} 1 - 0.02 D & D < 10 \text{ mm} \\ 0.8 & D \geq 10 \text{ mm} \end{cases} \quad (167)$$

However it is rare the case where there is only dry hail within the entire resolution volume. Below the iso-0°C altitude hailstones start to melt and therefore the radar resolution volume is composed of hailstones in various degrees of melting together with big water droplets.

High density melted hail can be approximated by a two body layer with an icy nucleus and a water coat. In lower density hail water first fills the air cavities in the hailstone and at a second stage the water coat is formed. Melting hail has typically a lower axis ratio than dry hailstones. The canting angle is also lower since the water coat tends to stabilize the hailstone. Ryzhkov et al. (2011) use experimental results of Rasmussen et al. (1984) to determine the axis ratio of melting hail as a function of the mass water fraction

$$r_{mh} = \begin{cases} r_{dh} - 5(r_{dh} - 0.8)f_{mw} & f_{mw} < 0.2 \\ 0.88 - 0.40f_{mw} & 0.2 \leq f_{mw} \leq 0.8 \\ 2.8 - 4r_w + 5(r_w - 0.56)f_{mw} & f_{mw} > 0.8 \end{cases} \quad (168)$$

It should be noticed that there is a limit on the amount of liquid water that a hailstone can contain. Predominantly liquid water drops are not larger than 8 mm because they break. Moreover only a certain amount of water can be contained in the water coat. Excess water sheds away. The maximum water that the hailstone can retain has empirically been determined to follow the following formula (Rasmussen and Heymsfield, 1987):

$$m_{wmax} = 0.268 + 0.1389 m_i [g] \quad (169)$$

Consequently, the maximum mass water fraction that can be sustained without shedding can be written as follows:

$$f_{mwmax} = \frac{m_w}{m_w + m_i} = \frac{0.268 + 0.1389 m_i}{0.268 + 1.1389 m_i} \quad (170)$$

Consequently, assuming the ice density to be that of pure ice (i.e. 0.0009167 g/mm³) and a typical particle diameter ranging between 5 and 50 mm the fraction mass water sustainable decreases with size from 0.821 to 0.125.

9.2 Particle size distribution

Experimental results by Cheng et al. (1985) show that hail close to the ground has the following empirical formula:

$$N(D) = C \Lambda^{4.11} e^{-\Lambda D} \quad (171)$$

With Λ varying from 0.1 to 1 mm⁻¹ and C from 60 to 300. This particle size will change with melting because due to the variation in particle diameter.

While melting the shed water will be accounted for assuming a gamma distribution with $\Lambda=2$ mm⁻¹ and $\mu=2$ and N_0 given by the total mass shed by all particles across the hailstone particle size distribution, i.e.:

$$m_t = \int_{D_{min}}^{D_{max}} m_{shed}(D) N(D) dD \quad (172)$$

$$N_{0shed} = \frac{m_t}{\int_{D_{min}}^{D_{max}} m_w(D) D^\mu e^{-\Lambda D} dD} \quad (173)$$

With $D_{max}=5$ mm.

9.3 Equivalent liquid water content

A similar procedure as the computation of snow equivalent liquid water content can be followed with hail. To that the shed water is added.

9.4 Equivalent rainfall rate

The terminal velocity of hail stones depend on the degree of melting. We follow here the approach by Ryzhkov et al. (2013). The Best number of hailstones is:

$$X = \frac{8 m g \rho_a}{\pi \eta^2} \quad (174)$$

Where m, g, ρ_a and η are the hailstone mass [Kg], the gravitational acceleration [ms⁻²], the air density [Kg m⁻³] and the dynamic viscosity of air [Kg m⁻¹s⁻¹]. The Reynolds number is then:

$$N_{\mathfrak{R}} = \begin{cases} 0.448 X^{0.5536} & X < 3.46e8 \\ \left(\frac{X}{0.6} \right)^{0.5} & X \geq 3.46e8 \end{cases} \quad (175)$$

For dry hailstones the terminal velocity is simply:

$$v_{dh} = \frac{\eta N_{\mathfrak{R}}}{\rho_a D} \left[\frac{m}{s} \right] \quad (176)$$

For hail stones that have melted up to the beginning of shedding the terminal velocity is:

$$v_{eq} = \begin{cases} \left(-0.1021 + 6.116e2 m^{1/3} - 1.469e4 m^{2/3} + 1.513e5 m - 5.584e5 m^{4/3} \right) \left(\frac{\rho_0}{\rho_a} \right)^{0.5} & N_{\mathfrak{R}} < 5000 \\ (4.80e3 + 4.832e6 m) \frac{\eta}{\rho_a D} \left(\frac{\rho_0}{\rho_a} \right)^{0.5} & 5000 \leq N_{\mathfrak{R}} < 25000 \\ v_{dh} & N_{\mathfrak{R}} \geq 25000 \end{cases} \quad (177)$$

The terminal velocity of the hailstone varies therefore between that of a dry hailstone and that where the water coat is completely formed and water starts shedding:

$$v_{mh} = v_{dh} + \frac{m_w}{m_{wmax}} (v_{eq} - v_{dh}) \quad (178)$$

And the equivalent rainfall rate can be computed as for snow.

9.5 Mass water fraction

The degree of melting depends on the heat transfer equations. The melting is computed as a function of height as follows:

$$\frac{dq}{dh} = \rho_i L_m \frac{dV_i}{dh} \quad (179)$$

Where ρ_i is the density of ice [Kg m^3], V_i is the ice core volume [m^3], dq/dh is the rate of change of enthalpy with height and L_m is the enthalpy defined in section 8.5.

The change of enthalpy depends on the size of the hailstone as follows:

$$\frac{dq}{dh} = \begin{cases} \frac{-4\pi D}{v_{mh} - v_w} \left(k_a (T_\infty - T_0) f_h + L_v D_v (\rho_{v,\infty} - \rho_{v,0}) f_v \right) & N_{\text{pr}} < 250 \\ \frac{-2\pi D}{v_{mh} - v_w} \left(k_a (T_\infty - T_0) f_h + L_v D_v (\rho_{v,\infty} - \rho_{v,0}) f_v \right) & 250 \leq N_{\text{pr}} \leq 3000 \\ \frac{2\pi D D_i k_w (T_0 - T_a)}{(v_{mh} - v_w)(D - D_i)} = \frac{-2\pi D}{v_{mh} - v_w} \left(k_a (T_\infty - T_a) f_h + L_v D_v (\rho_{v,\infty} - \rho_{v,a}) f_v \right) & 3000 \leq N_{\text{pr}} \leq 6000 \\ \frac{-0.76\pi D_i N_{\text{pr}}^{1/2}}{v_{mh} - v_w} \left(N_{\text{pr}}^{1/3} k_a (T_\infty - T_0) + N_{\text{sc}}^{1/3} L_v D_v (\rho_{v,\infty} - \rho_{v,0}) \right) & 6000 \leq N_{\text{pr}} \leq 2e4 \\ \frac{-(0.57 + 9e-6 N_{\text{pr}}) \pi D_i N_{\text{pr}}^{1/2}}{v_{mh} - v_w} \left(N_{\text{pr}}^{1/3} k_a (T_\infty - T_0) + N_{\text{sc}}^{1/3} L_v D_v (\rho_{v,\infty} - \rho_{v,0}) \right) & N_{\text{pr}} > 2e4 \end{cases} \quad (180)$$

Here T_∞ is the air temperature far away from the hailstone, T_0 is the reference 0°C temperature in K (i.e. $T_0=273.15$ K) and T_a is the temperature at the surface of the particle which is found solving numerically the equation. $\rho_{v,\infty}$ is the water vapor density at temperature T_a , $\rho_{v,0}$ is the water vapor density at temperature T_0 and $\rho_{v,a}$ is the water vapor density at temperature T_a . The water vapor density can be written as a function of saturated vapor pressure and relative humidity as:

$$\rho_v = \frac{RH}{100} \frac{M_w}{R} \frac{e_{\text{sat},w}(T)}{T} \left[\frac{\text{Kg}}{\text{m}^3} \right] \quad (181)$$

D is the equivalent diameter of the hailstone [m] while D_i is the equivalent diameter of the ice core. k_a is the thermal conductivity of air given by . L_v is the latent enthalpy of vaporization and D_v is the diffusivity of water vapor in air defined in section 8.5.

k_w is the thermal conductivity of water:

$$k_w = 0.568 e^{0.003473(T_\infty - T_0) - 3.823e-5(T_\infty - T_0)^2 + 1.087e-6(T_\infty - T_0)^3}$$

f_h is the thermal ventilation coefficient:

$$f_h = 0.78 + 0.308 N_{\text{pr}}^{1/3} N_{\text{pr}}^{1/2} \quad (182)$$

Where N_{pr} is the Prandtl number:

$$N_{\text{pr}} = \frac{\eta}{\rho_a} \frac{1}{K_a} \quad (183)$$

Here K_a is the thermal diffusivity of air:

$$K_a = 9.1018e-11 T_\infty^2 + 8.8197e-8 T_\infty - 1.0654e-5 \left[\frac{\text{m}^2}{\text{s}} \right] \quad (184)$$

f_v is the vapor ventilation coefficient:

$$f_v = 0.78 + 0.308 N_{\text{sc}}^{1/3} N_{\text{pr}}^{1/2} \quad (185)$$

Where N_{Sc} is the Schmidt number defined in section 8.5.

From the lost ice volume, the lost ice mass is obtained as:

$$\frac{dm_i}{dh} = \rho_i \frac{dV_i}{dh} = \frac{1}{L_m} \frac{dq}{dh} \quad (186)$$

As in section 8.5, by conservation of the mass a loss of ice mass corresponds to a gain in water mass although it should be noticed that mass conservation holds only up to the onset of water shedding. Again, as in section 8.5, to obtain the fraction mass water at a specific altitude we have to integrate along the path between the iso-0°C altitude and the current altitude.

9.6 Refractive index

For high ice density hail the particle has to be computed as a two layer body: an ice core with ice refractivity which can be computed in the same manner as for ice crystals and a water coat.

For low density ice the situation is more complex. Initially water fills in the air cavities and in such case the particle should be considered a uniform mixture of low density ice and water. Once the air cavities are soaked a water coating is formed and therefore the particle has to be seen as a two layer body.

9.7 Vertical column

There is a substantial overlap between hail and heavy rain which could result in some radar bins being arbitrarily classified as rain and others as hail within the same vertical column, which, unless it melts completely before reaching the surface, should not be the case.

Considering the potential risks posed by hail both for the infrastructure and for a correct estimation of rainfall rate if a radar bin is signaled as hail all the bins in the column below the confirmed hail classification should be classified as well as hail albeit with a lower probability.

Chapter 10 Simulation of graupel/melting graupel

10.1 Particle shape

Graupel can be formed by two different processes: In summer the process is similar to that of the formation of hail, simply the updraft may be weaker and therefore the size of the stones is smaller, maximum 5 mm. In winter it may be due to a thermal inversion. Snowflakes melt when they cross the highest iso-0° altitude and refreeze rapidly when they cross the second iso-0° position. In summer, therefore graupel can exist in a partially melted form while in winter graupel may be completely frozen on the ground.

As in the case of hail, graupel tends to a spherical shape with high axis ratio, typically 0.7-0.8. When melting and after soaking it will tend to the shape of an equivalent droplet at a rate proportional on the mass water fraction.

10.2 Particle size distribution

We will use the same particle distribution as for hail but the maximum size will be limited to 5 mm.

10.3 Equivalent liquid water content

It can be computed in a similar way as for hail.

10.4 Equivalent rainfall rate

The same equations as for hail/melting hail apply. Simply the size of the particle is going to be smaller.

10.5 Refractive index

Respect to hail, graupel is less dense. Therefore, at the onset of the melting the two layer model does not apply because water tends to fill in the air cavities first. Only when the air cavities are filled a water layer is formed. Therefore we will model the particle as a snow with water inclusions when starting to melt on only in a later melting stage we will use the two layer model.

Chapter 11 Simulation results

We will try to summarize here some simulation results. The simulations are performed at C-band and for the 20 elevations that constitute the volume scan of the MeteoSwiss radars. We will show here the results of the simulations performed at 0.4° elevation.

11.1 Single particle scattering

11.1.1 Ice crystals

The scattering properties of ice crystals are very different depending on the crystal habit (See Fig. 5 to Fig. 7). Small, spherical-like particles have very low backscatter cross section which is virtually the same for both H and V and very low values of Kdp, extinction and δ_{co} while the value of ρ_{hv} is rather high. The backscatter cross section of plates have much larger differences between H and V and lower ρ_{hv} . Although they have a lower axis ratio, due to the lower density dendrites have a smaller backscatter cross section difference between H and V than plates.

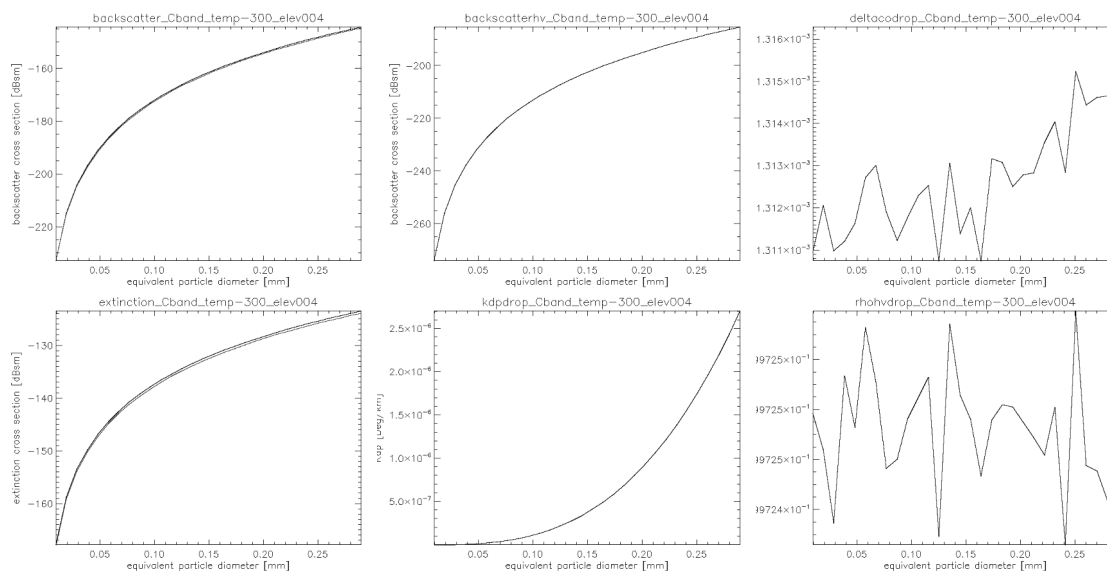


Fig. 5 Scattering properties of individual ice crystals at -30°C (spherical particles)

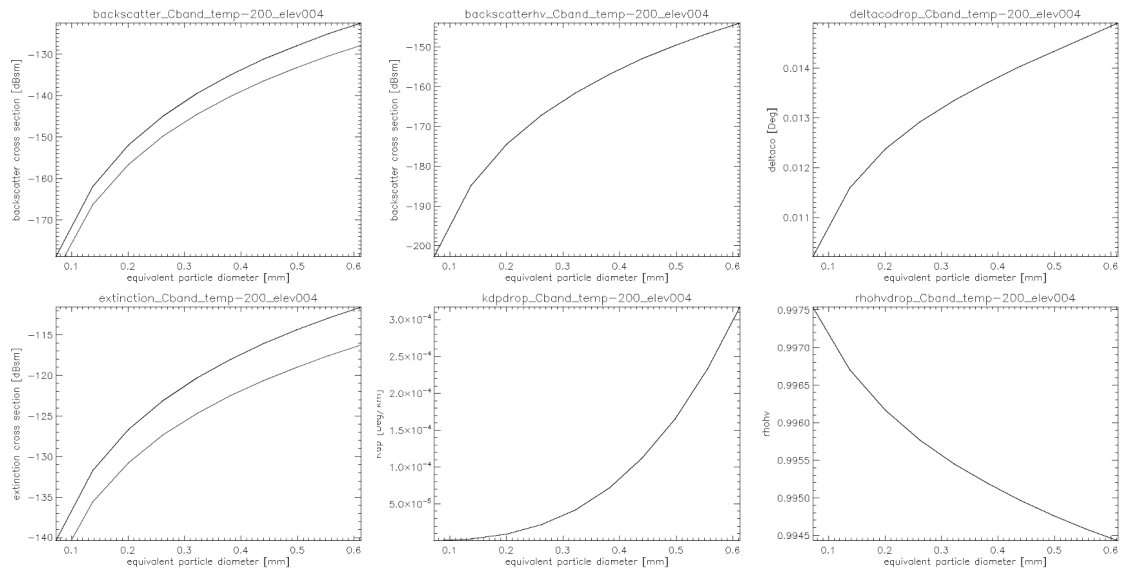


Fig. 6 Scattering properties of individual ice crystals at -20°C (Hexagonal plates)

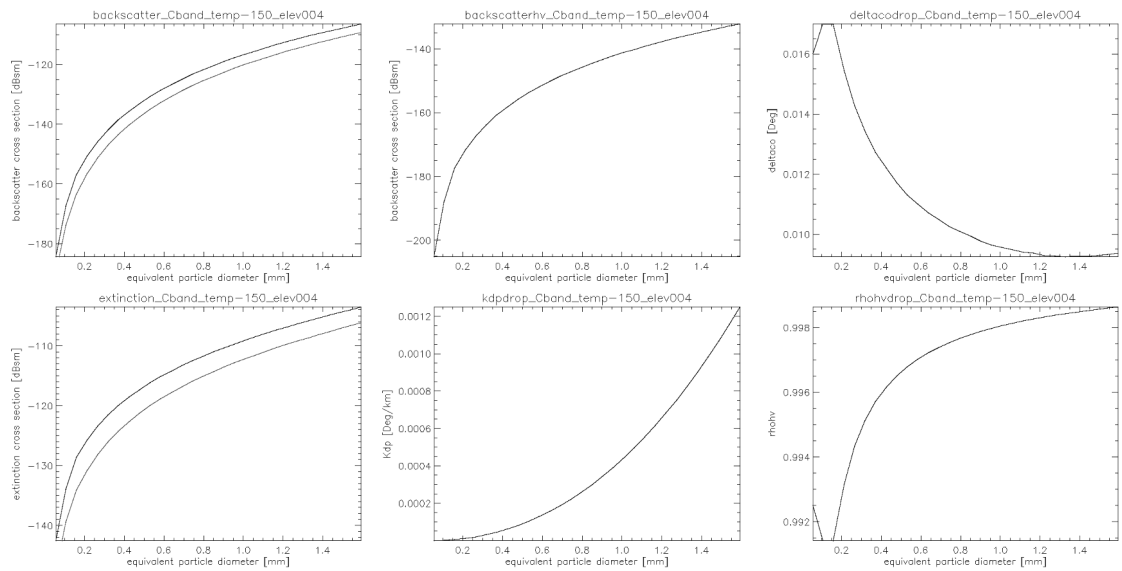


Fig. 7 Scattering properties of individual ice crystals at -15°C (dendrites)

11.1.2 Dry snow

Snowflakes (see Fig. 8) have very high ρ_{hv} and very low KDP and a small difference between the backscatter cross-section of H and V.

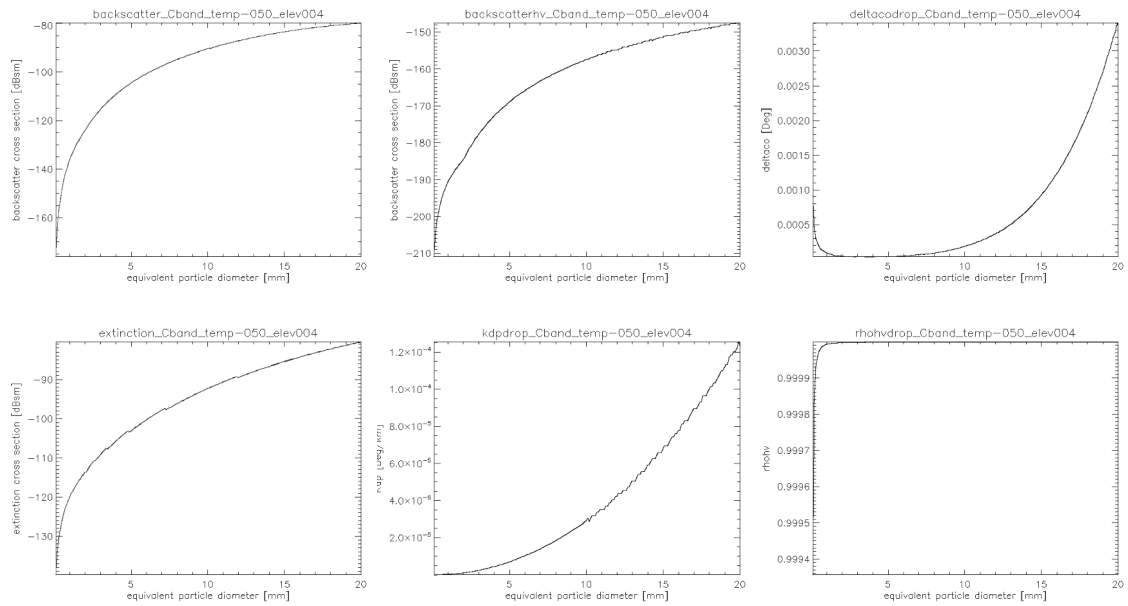


Fig. 8 Scattering properties of individual snowflakes

11.1.3 Wet snow

Wet snow (Fig. 9 and Fig. 10) exhibit a transition from the properties of dry snow to the properties of rain. KDP and δ_{co} gradually increase while ρ_{hv} decreases. Notice that the size of the snowflakes diminishes with increasing melting.

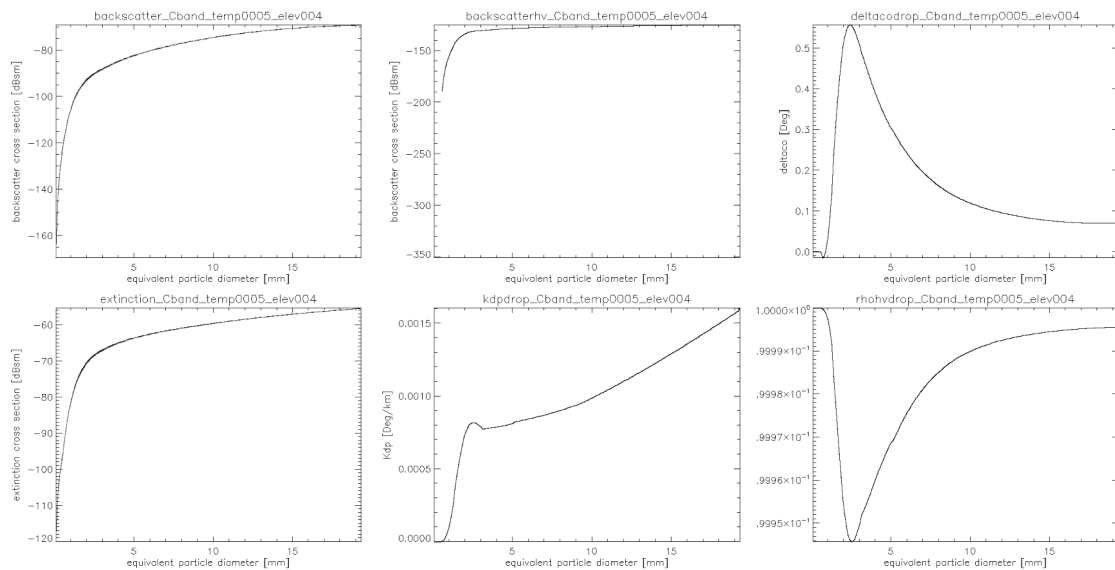


Fig. 9 Scattering properties of individual melting snowflakes at 0.5°C

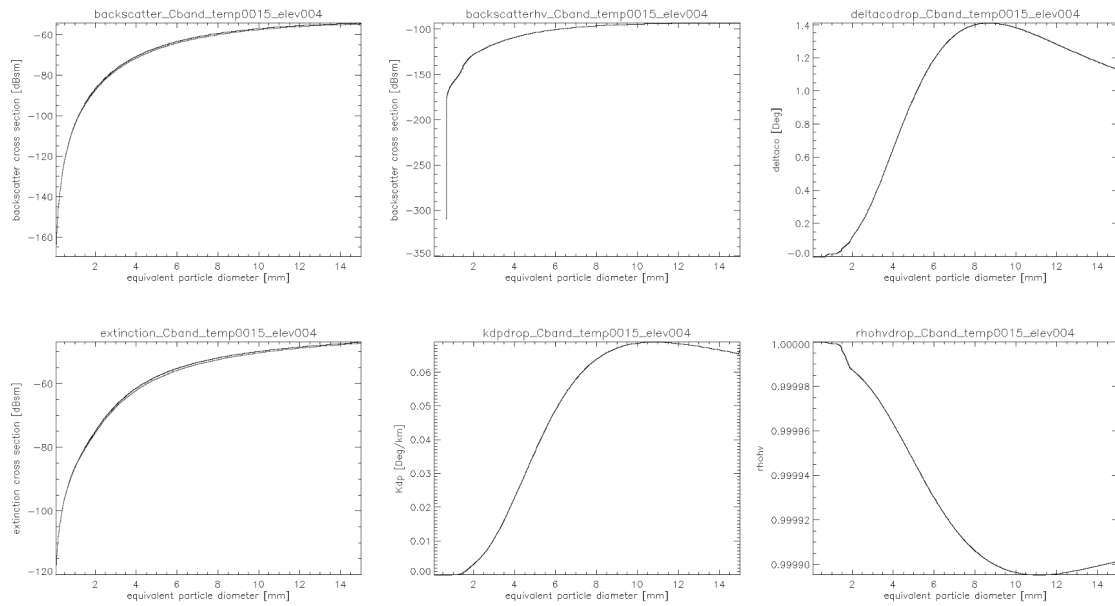


Fig. 10 Scattering properties of individual melting snowflakes at 1.5°C.

11.1.4 Rain

In our simulations (Fig. 11 and Fig. 12) we use the same bin width as that of the PARSIVEL disdrometer. That may result in an excessively coarse simulation for the larger rain drops (where resonant effects are present) as can be observed from the plots of δ_{co} and KDP. It should be noticed that, contrary to solid precipitation, the scattering properties change significantly with temperature. In particular, there is a significant increase of δ_{co} and KDP and a decrease in ρ_{hv} with temperature.

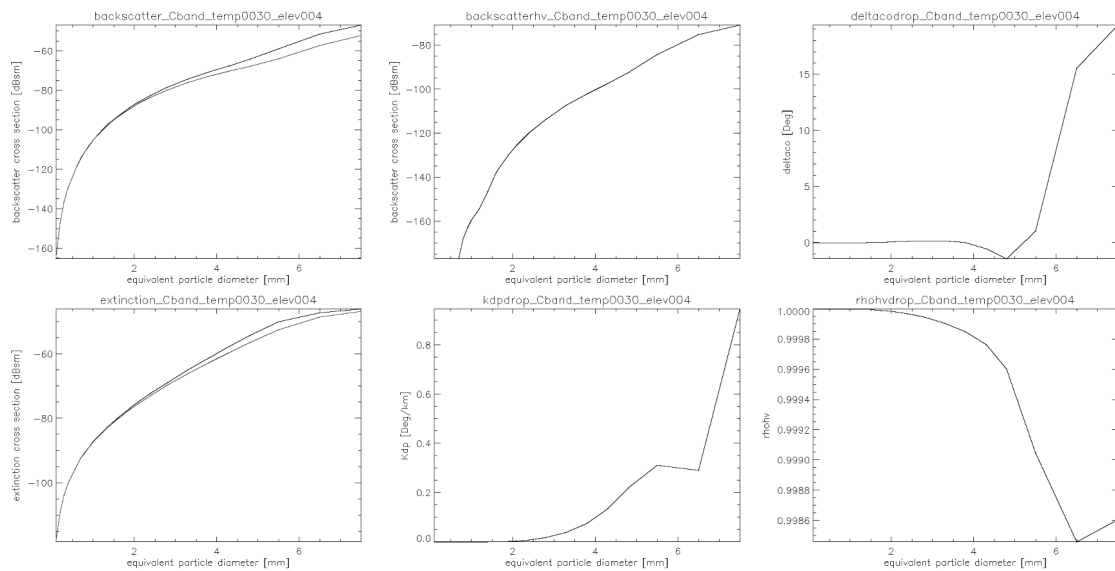


Fig. 11 Scattering properties of individual raindrops at 3°C.

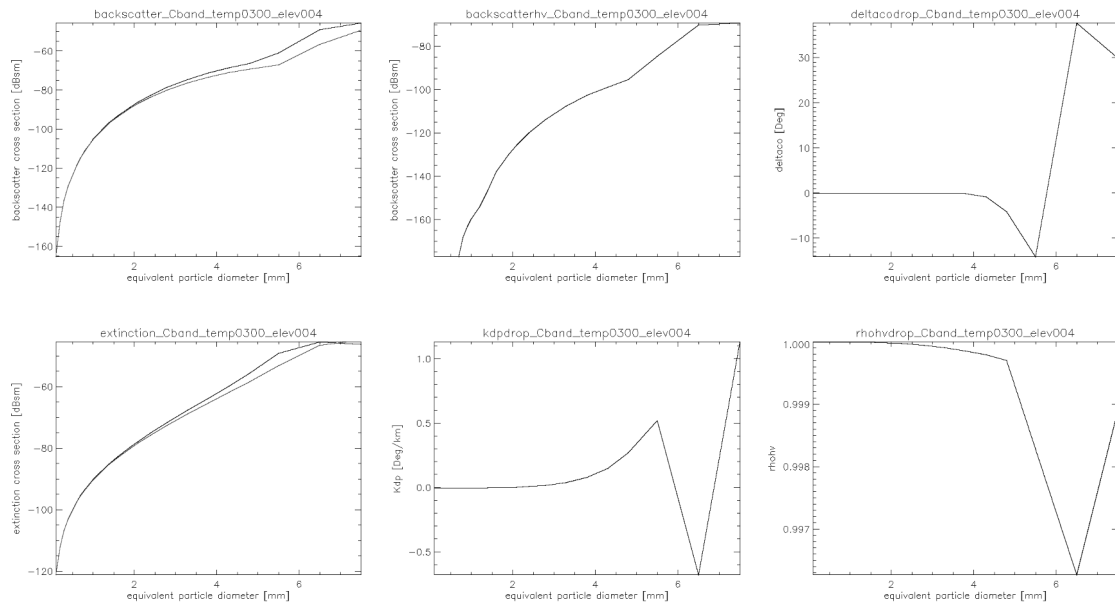


Fig. 12 Scattering properties of individual raindrops at 30°C

11.1.5 Graupel

Completely frozen graupel has similar properties than that of snow although with higher backscatter cross section for the same particle size due to graupel being denser (see Fig. 13). When it starts to melt though (Fig. 14 and Fig. 15) the scattering properties are becoming more complex following the transition from solid precipitation to rain.

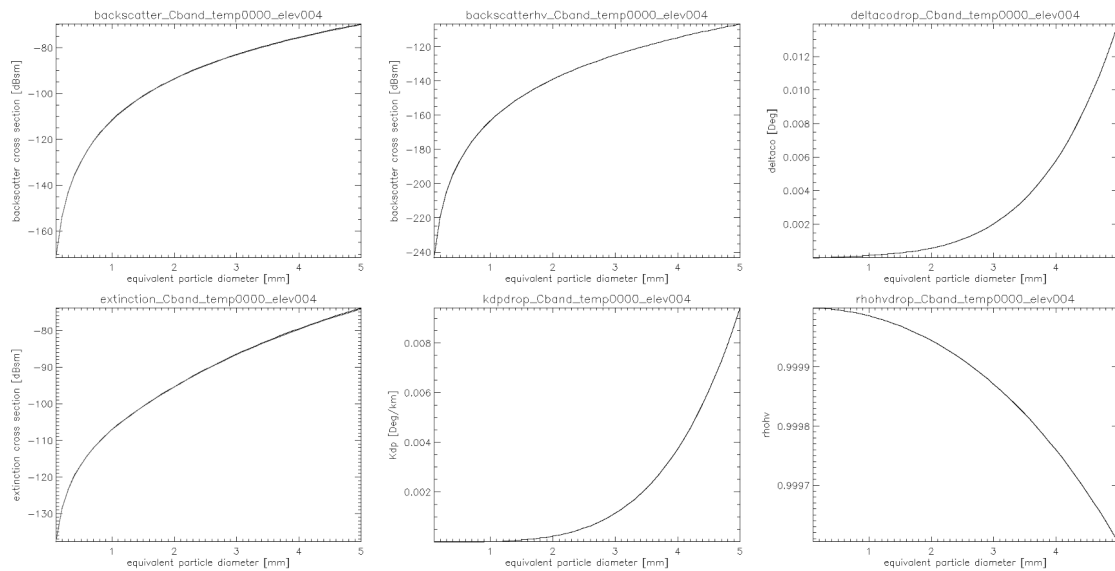


Fig. 13 Scattering properties of individual graupel at 0°C (no melting)

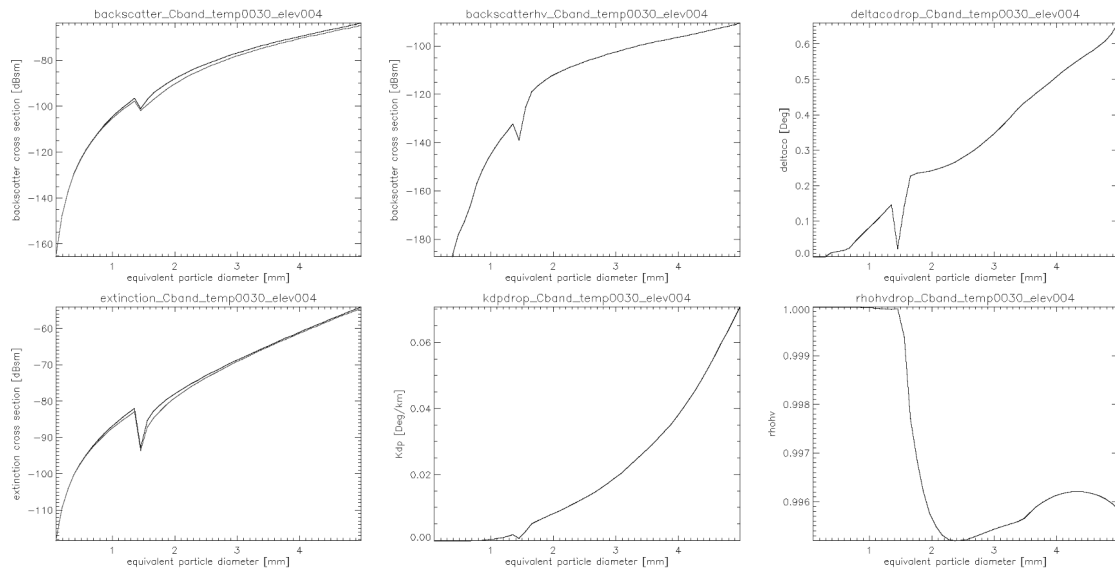


Fig. 14 Scattering properties of individual graupel at 3°C

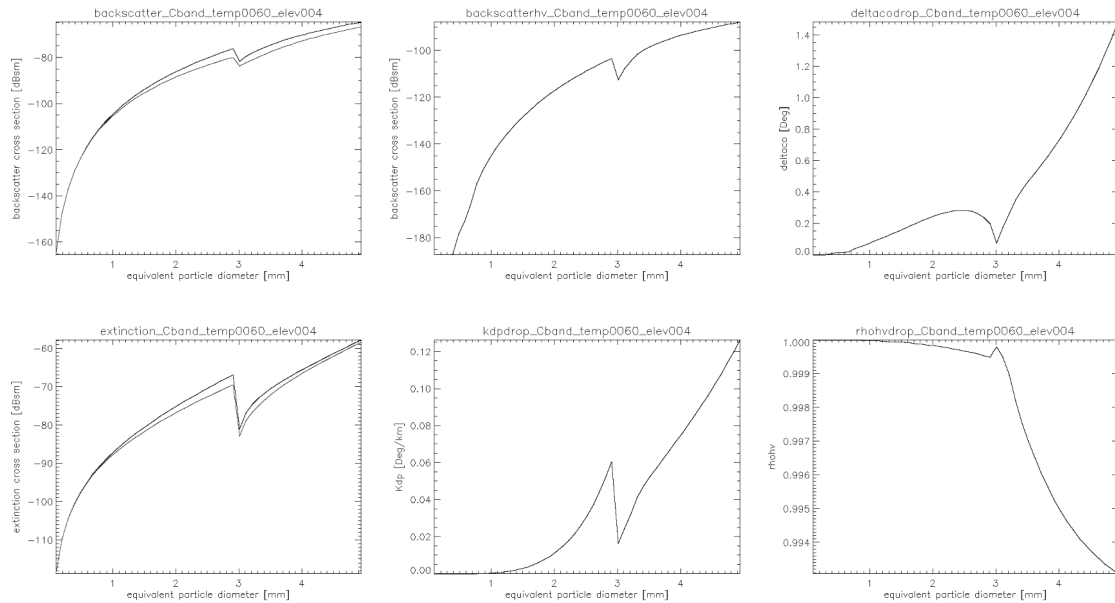


Fig. 15 Scattering properties of individual graupel at 6°C

11.1.6 Hail

The scattering properties of individual hailstones exhibit resonant effects for the larger sizes (see Fig. 16) with a decrease of ρ_{hv} , an increase of δ_{∞} and negative values of KDP. The melting of the hailstones adds complexity to the backscattering properties (see Fig. 17 to Fig. 19).

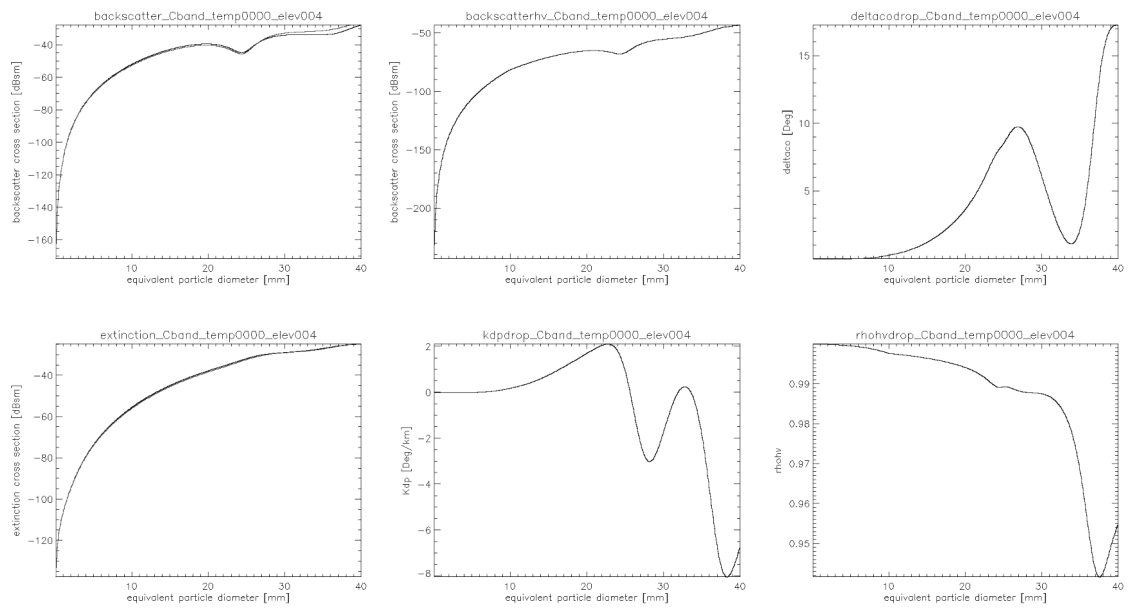


Fig. 16 Scattering properties of individual hailstones at 0°C (no melting)

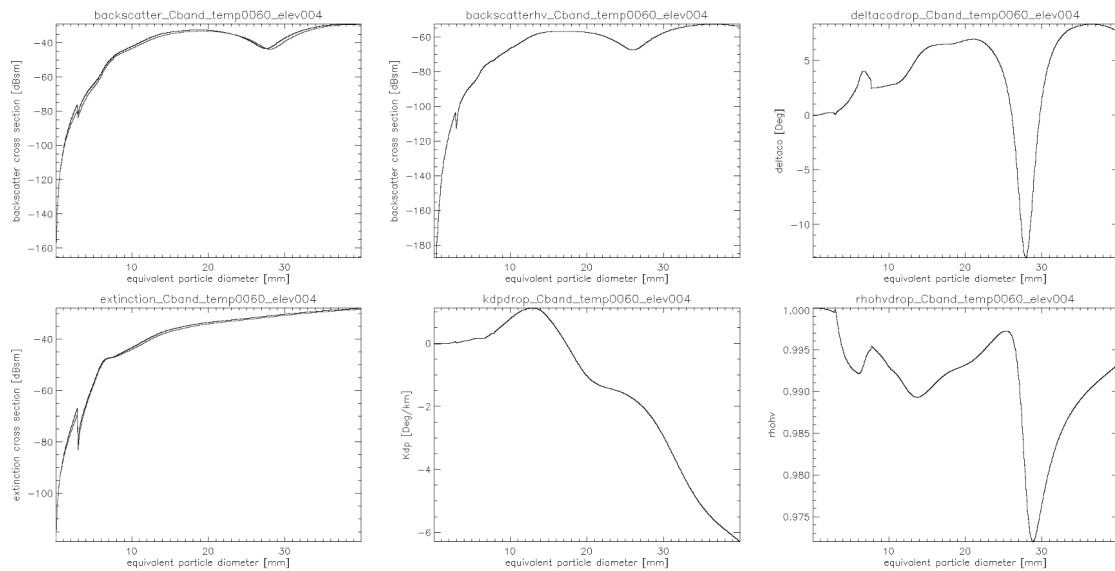


Fig. 17 Scattering properties of individual hailstones at 6°C

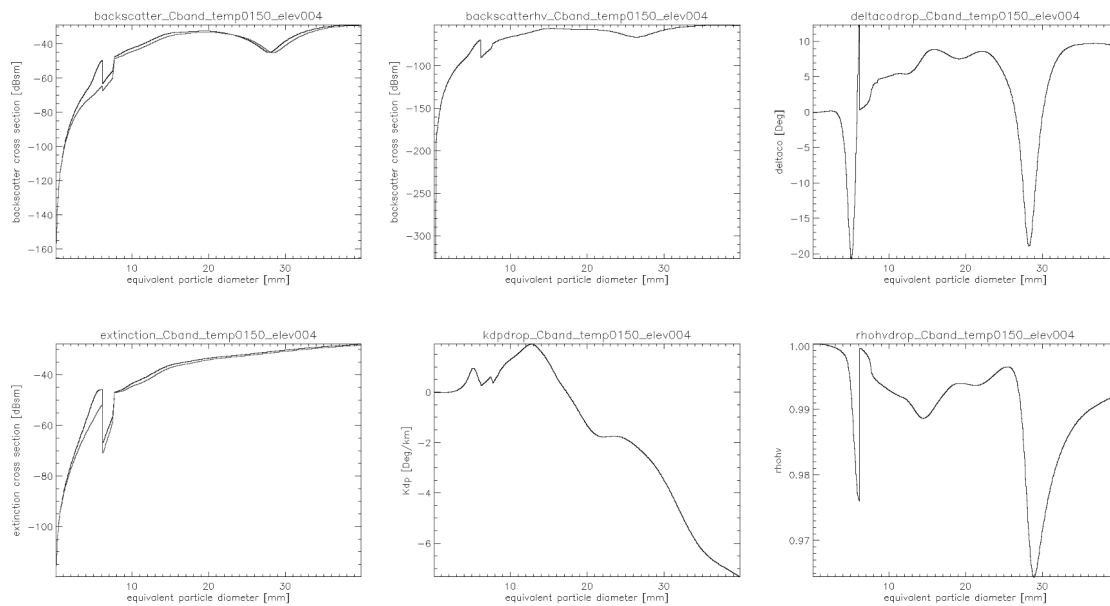


Fig. 18 Scattering properties of individual hailstones at 15°C

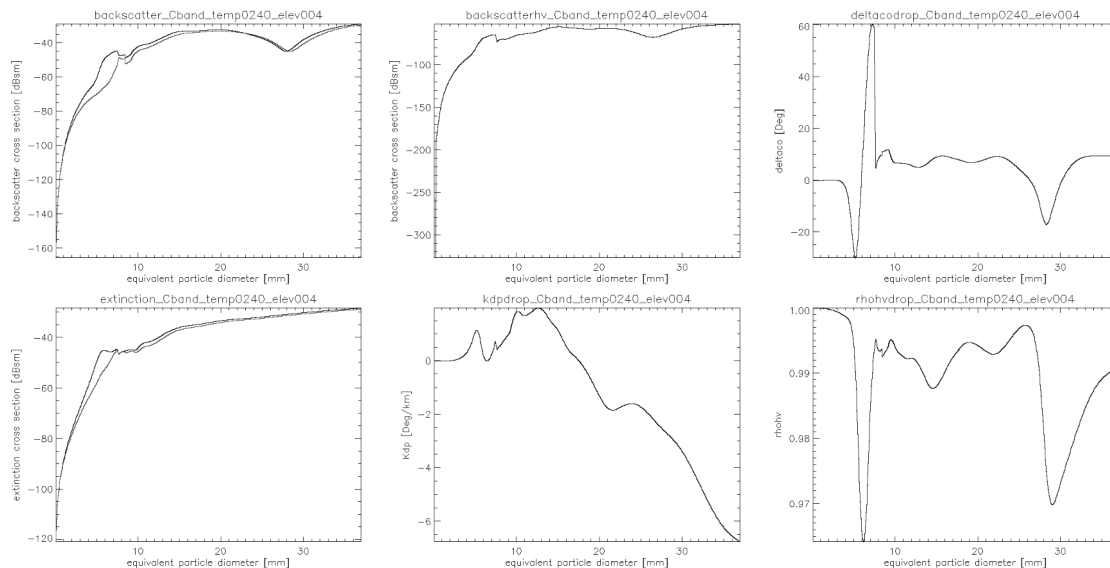


Fig. 19 Scattering properties of individual hailstones at 24°C.

11.2 Bulk hydrometeor scattering

11.2.1 Ice crystals

Fig. 20 presents the bulk scattering properties of ice crystals. It can be seen that they are characterized by virtually no attenuation, weak to moderate reflectivity, increasing KDP with reflectivity and highly variable Z_{dr} depending on the predominant crystal habit. From the simulations it can be seen that it is not reasonable to consider completely separate crystal habits. A particular crystal type can indeed be dominant but a mixture of several types of ice crystals is more likely. It should be noticed that the attenuation is very low while K_{dp} can be significantly high. Therefore there is no

correlation between K_{dp} and attenuation and attenuation correction techniques based on ϕ_{dp} should not be applied in areas of ice crystals.

As for the relation between polarimetric variables and equivalent rainfall rate (Fig. 21) it can be seen that both K_{dp} and Z_h can provide information. However, large uncertainty should be expected due to the presence of different crystal types in the same radar resolution volume.

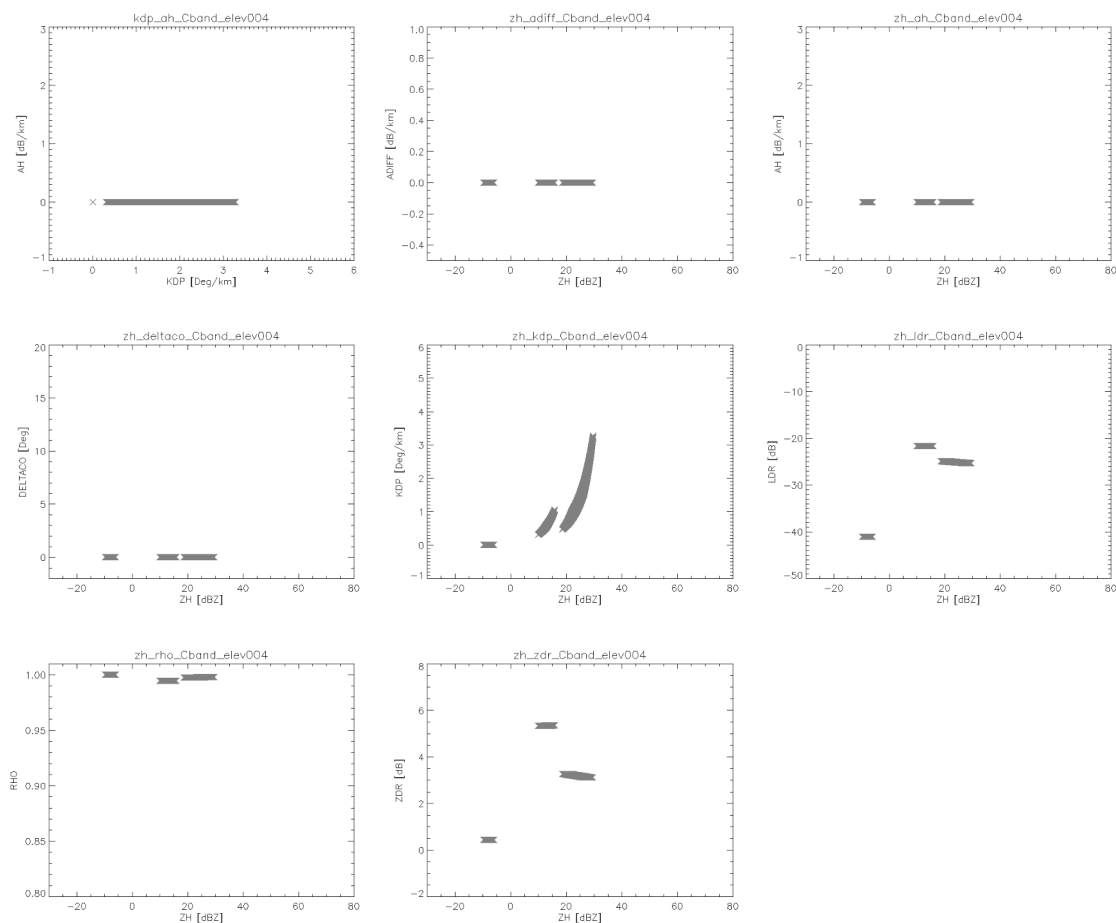


Fig. 20 Bulk scattering properties of ice crystals (different crystal habits put together)

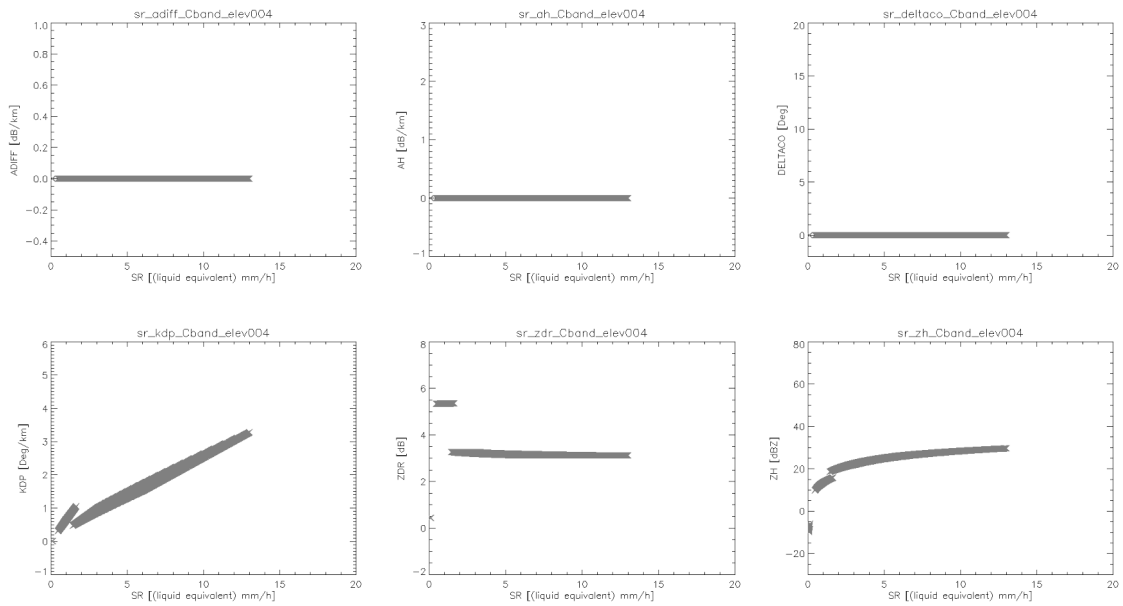


Fig. 21 Relationship between equivalent rainfall rate and polarimetric parameters for ice crystals

11.2.2 Dry snow

Dry snow is characterized by weak to moderate reflectivity, low attenuation, low KDP and high ρ_{hv} .

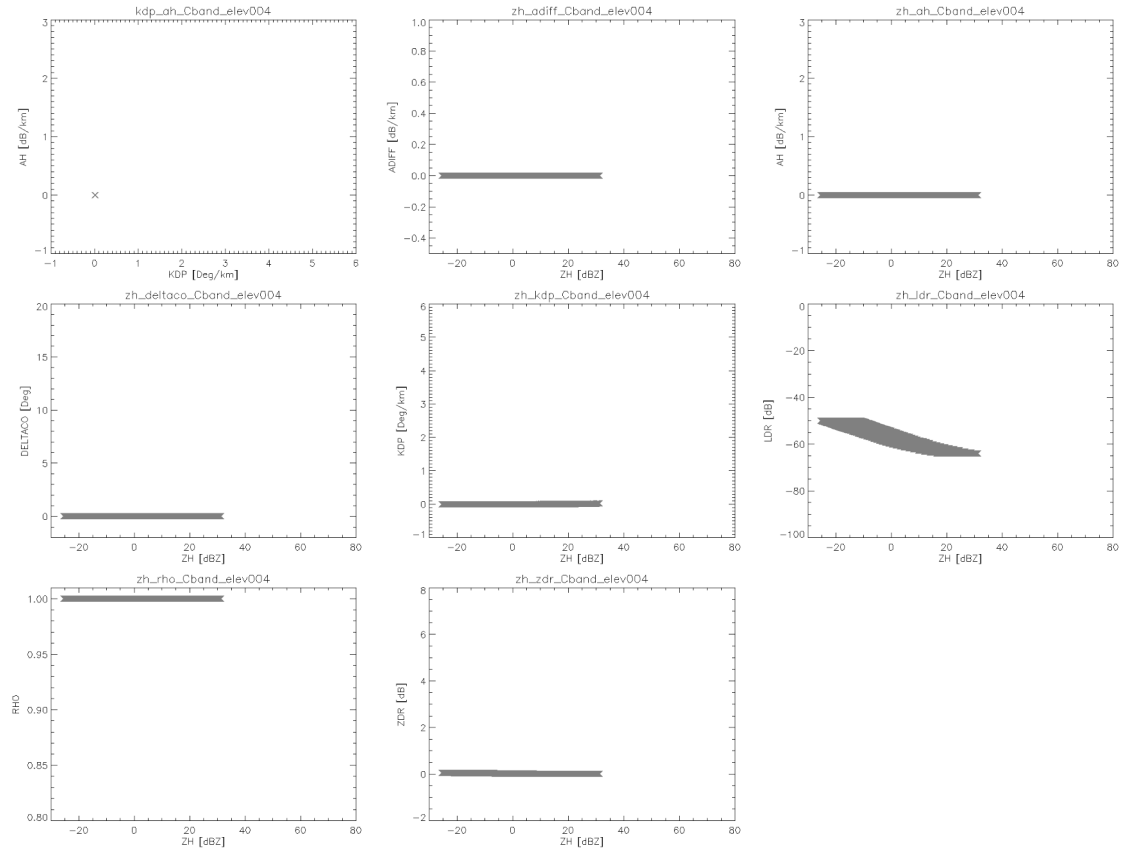


Fig. 22 Bulk scattering properties of dry snow

The only polarimetric variable that has significant variation with equivalent rainfall is reflectivity (see Fig. 23).

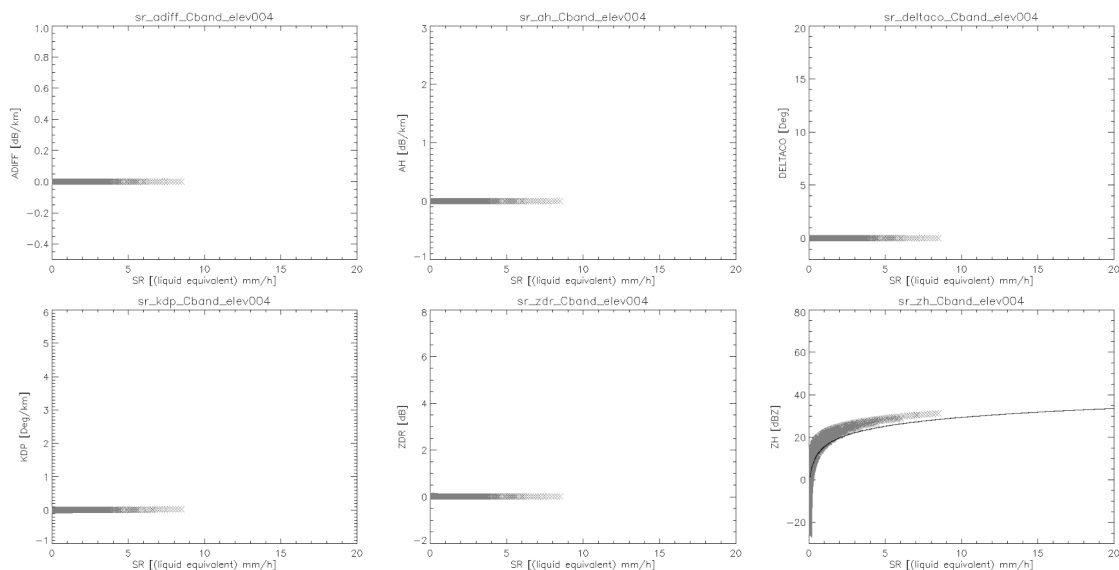


Fig. 23 Relationship between equivalent rainfall rate and polarimetric parameters for dry snow

11.2.3 Wet snow

Wet snow is characterized by large attenuation and differential attenuation, significant values of δ_{co} and KDP and increasing Z_{dr} (See Fig. 24). Although, it is known that the melting layer is characterized as well by a sharp decrease in ρ_{hv} our simulations have not captured that, likely due to the impossibility of characterizing the irregularities of the snowflake surface. Due to the different degrees of melting the scatter is significant.

As for the relationship between equivalent rainfall rate and polarimetric variables (Fig. 25) it is characterized by a very large scatter so that if a single variable is used to compute the rainfall rate the uncertainty can be quite large. However, a combination of different variables may decrease the uncertainty.

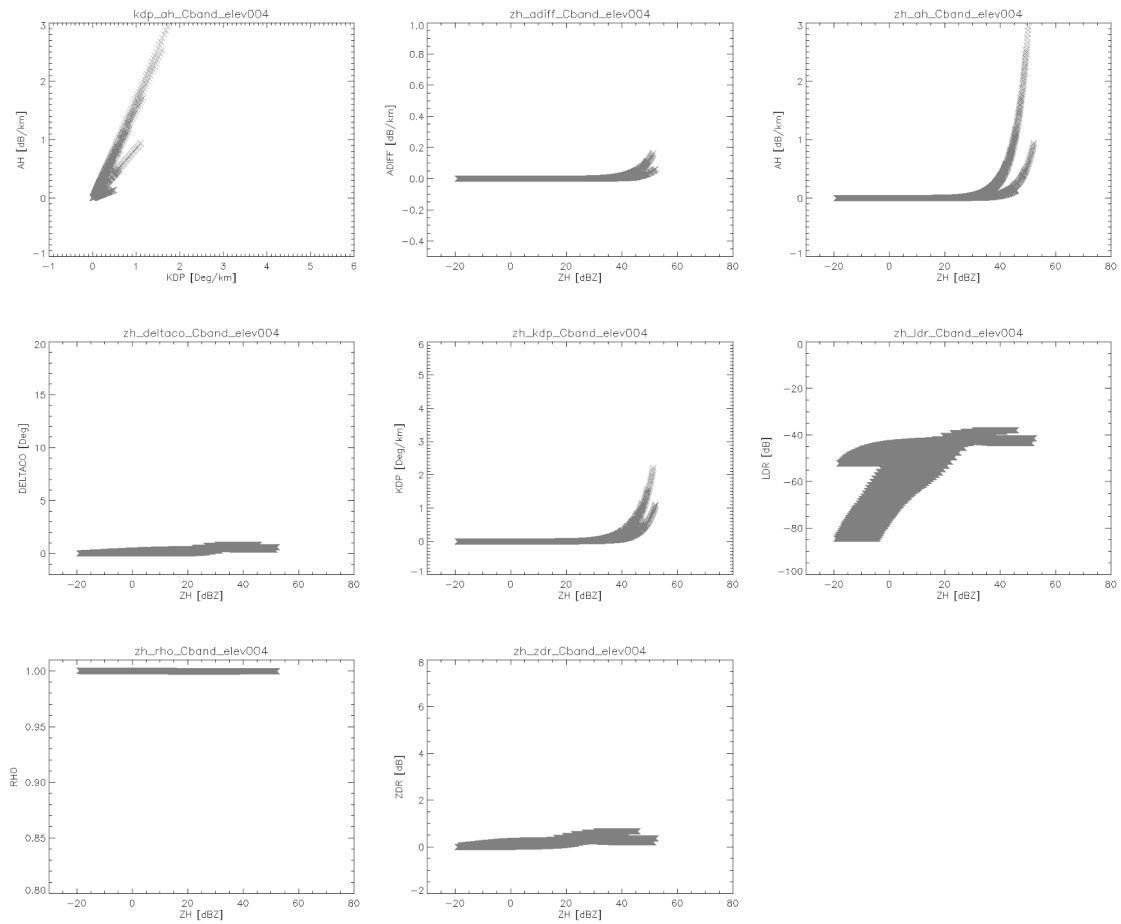


Fig. 24 Bulk scattering properties of wet snow

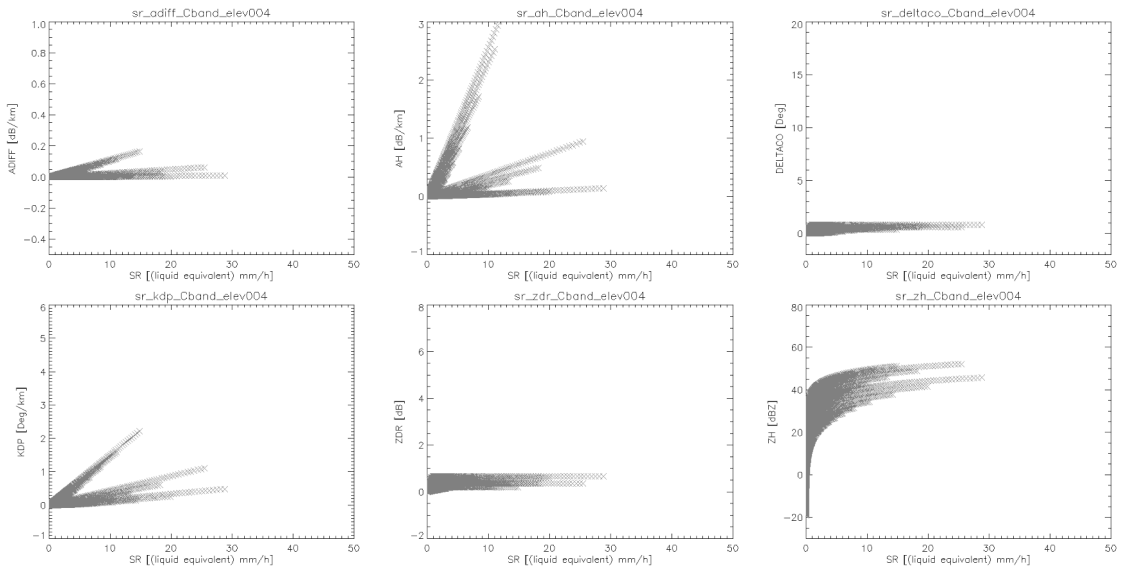


Fig. 25 Relationship between polarimetric variables and equivalent rainfall rate for wet snow

11.2.4 Rain

Our simulations of rainfall rate (Fig. 26) are not based on idealized DSD such as gamma or exponential but rather on actual PARSIVEL disdrometer measurements. That may be the reason of the significant scattering observable in the polarimetric variables relations, particularly for Z_{dr} , ρ_{hv} and δ_{co} . These parameters have been shown to be highly dependent on drop size and few large drops may have a significant impact. It is noticeable the high values of δ_{co} , which may affect the estimation of ϕ_{dp} .

As for the relationship between rainfall rate and polarimetric variables it can be observed that there is far less scatter using KDP or the attenuation. Therefore if these variables can be estimated accurately they should be favored for quantitative measurements.

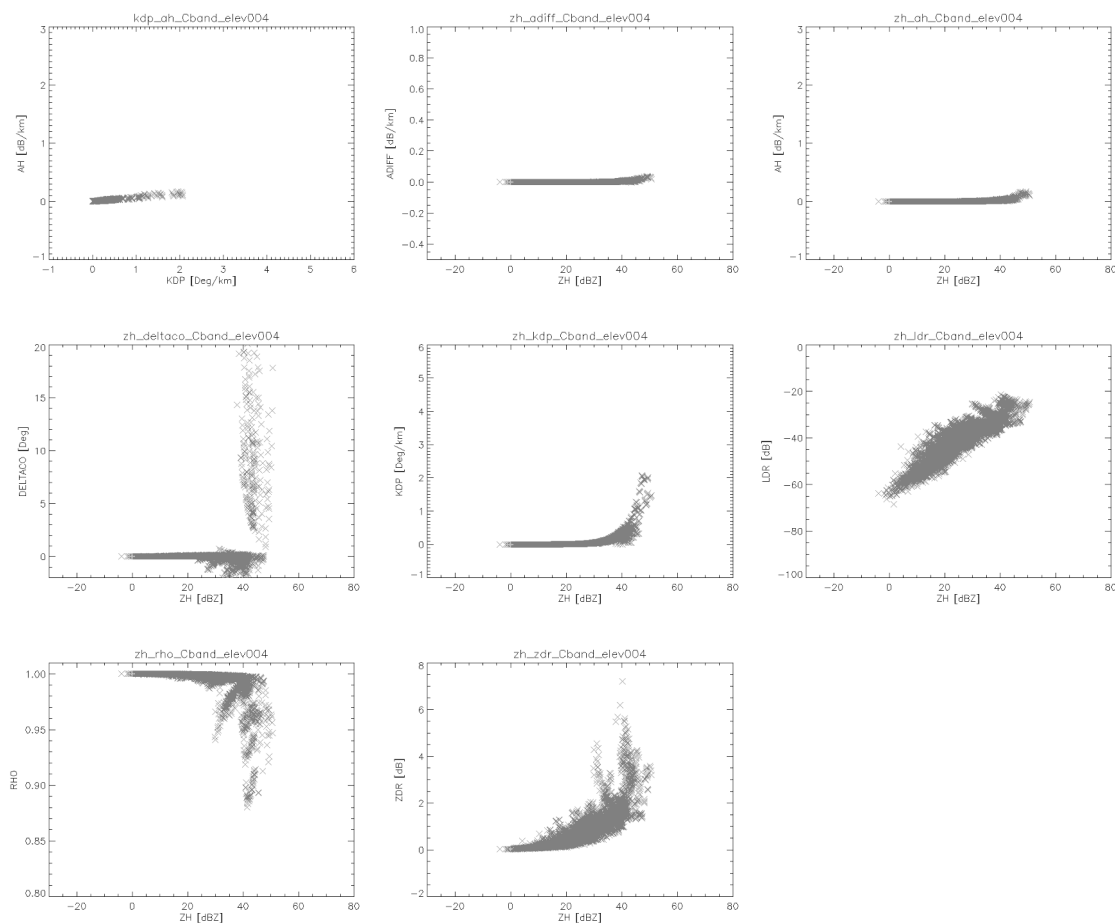


Fig. 26 Bulk scattering properties of rain

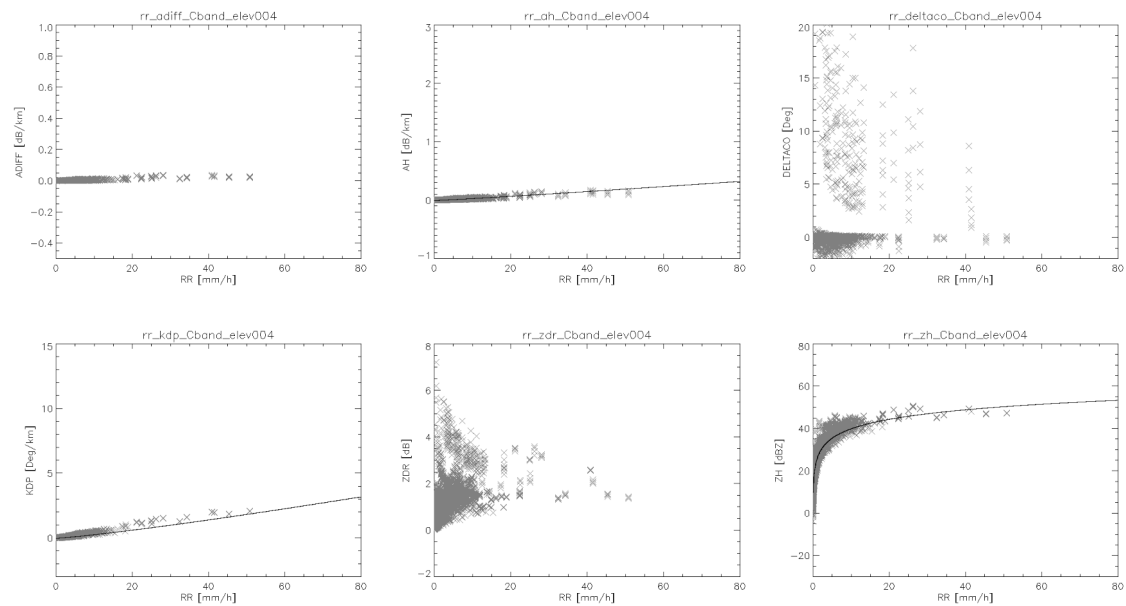


Fig. 27 Relationship between rainfall rate and polarimetric variables

11.2.5 Graupel

Graupel (Fig. 28) is characterized by small attenuation and differential attenuation, high KDP, significant δ_{co} and increasing Z_{dr} with increased degree of melting. The reflectivity levels are moderate.

As for the relationship between equivalent rainfall rate and polarimetric variables (Fig. 29) it is highly sensitive to the degree of melting and therefore large uncertainty should be expected.

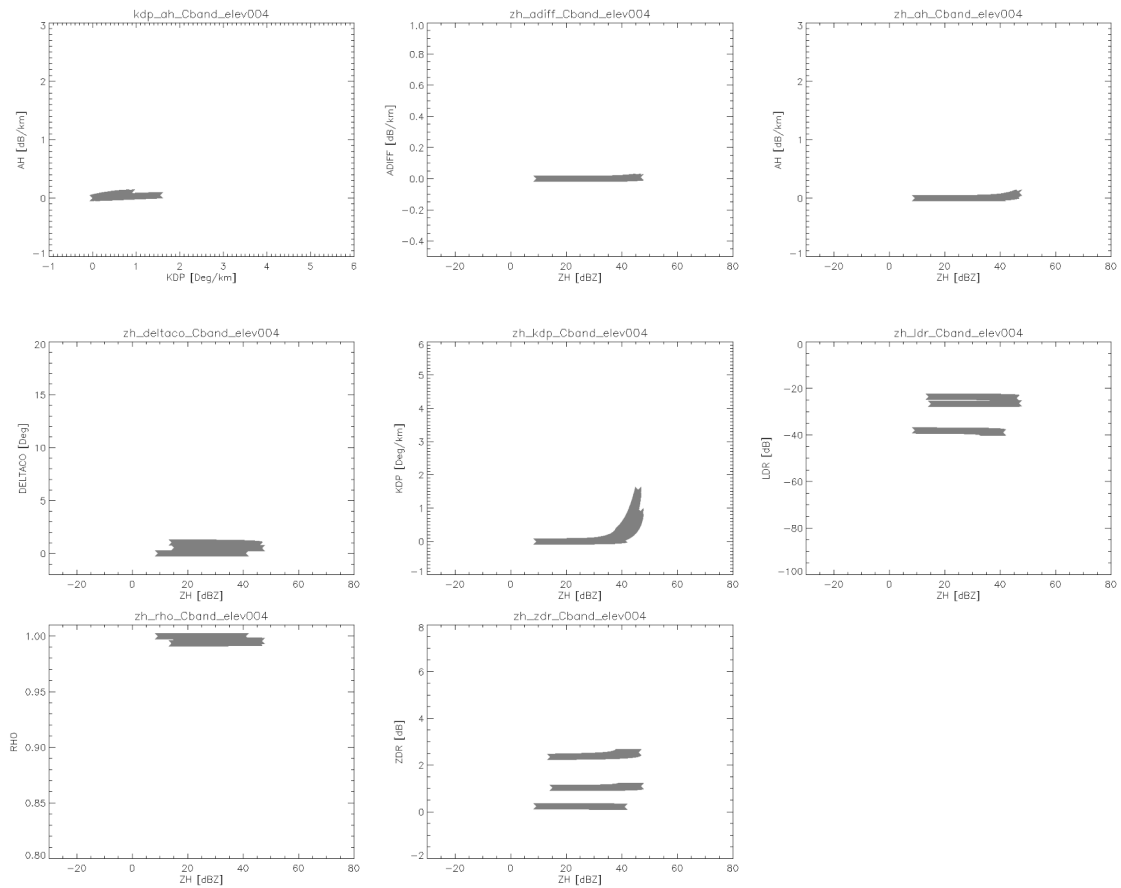


Fig. 28 Bulk scattering properties of graupel

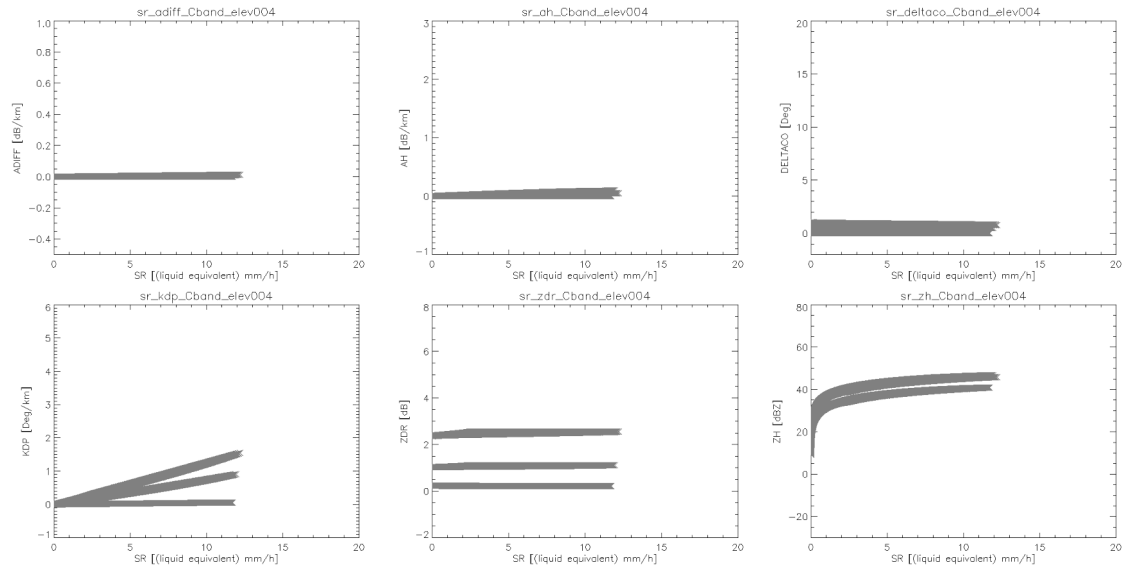


Fig. 29 Relationship between equivalent rainfall rate and polarimetric variables for graupel

11.2.6 Hail

Melting hail at C-band is characterized by extremely high reflectivity, Z_{dr} and KDP and low p_{hv} values (see Fig. 30). δ_{co} is also extremely high. As for the relationship between equivalent rainfall rate and

polarimetric variables, the spread is so huge that quantitative estimation of precipitation may not be possible and indicators like hail severity should be favored instead.

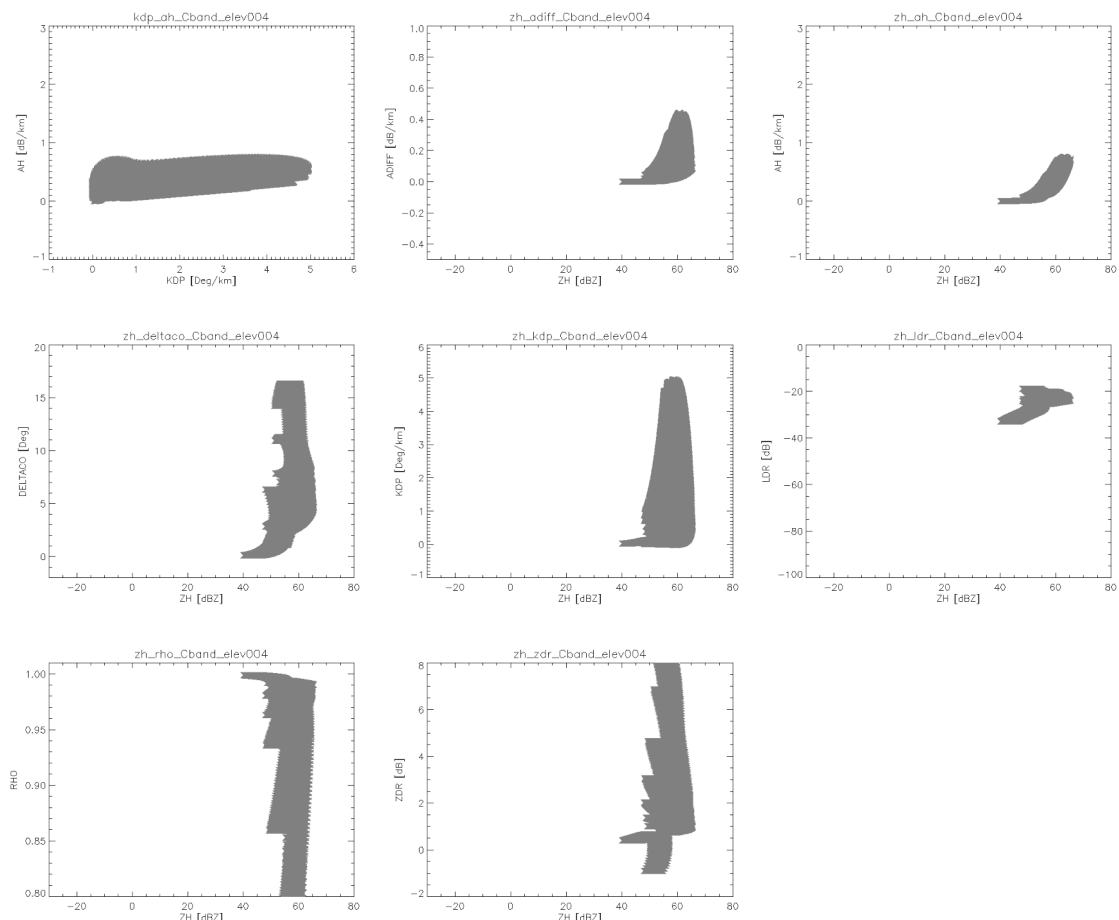


Fig. 30 Bulk scattering properties of hail

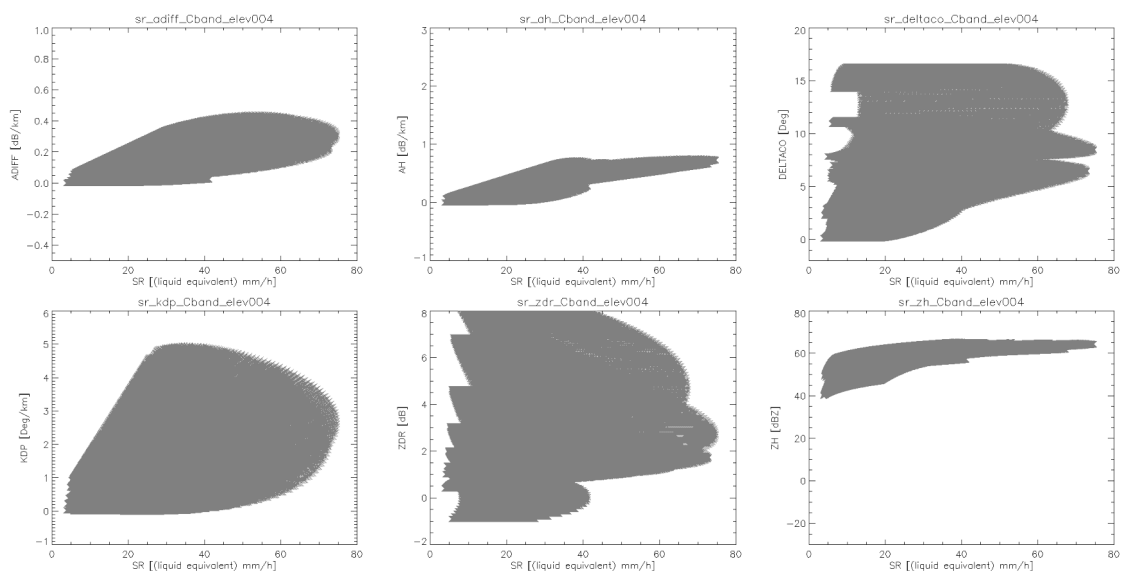


Fig. 31 Relationship between equivalent rainfall rate and polarimetric variables for hail

11.3 Membership Functions

The membership functions intended for use in the hydrometeor classification are two dimensional relationships between reflectivity and differential specific differential phase, co-polar correlation coefficient and differential reflectivity respectively. Fig. 32 presents an example of such membership functions as directly derived from simulations. It can be seen that hail is relatively easy to discriminate due to the large values of the polarimetric variables. Generally speaking, it is also relatively easy to discriminate between ice crystals and dry snow due to the higher KDP and Z_{dr} values with relatively low reflectivity although it is harder to discriminate with the very small ice particles present on top of the cloud and in such case temperature should be used to discriminate between graupel and ice crystals. It is much more difficult to discriminate between rain, melting snow and graupel/melting graupel on a gate by gate basis. Consequently an algorithm to detect the extend of the melting layer should be implemented. Finally, as it can be seen from the membership functions even at high elevation angle there is sufficient polarimetric information to attempt an hydrometeor classification.

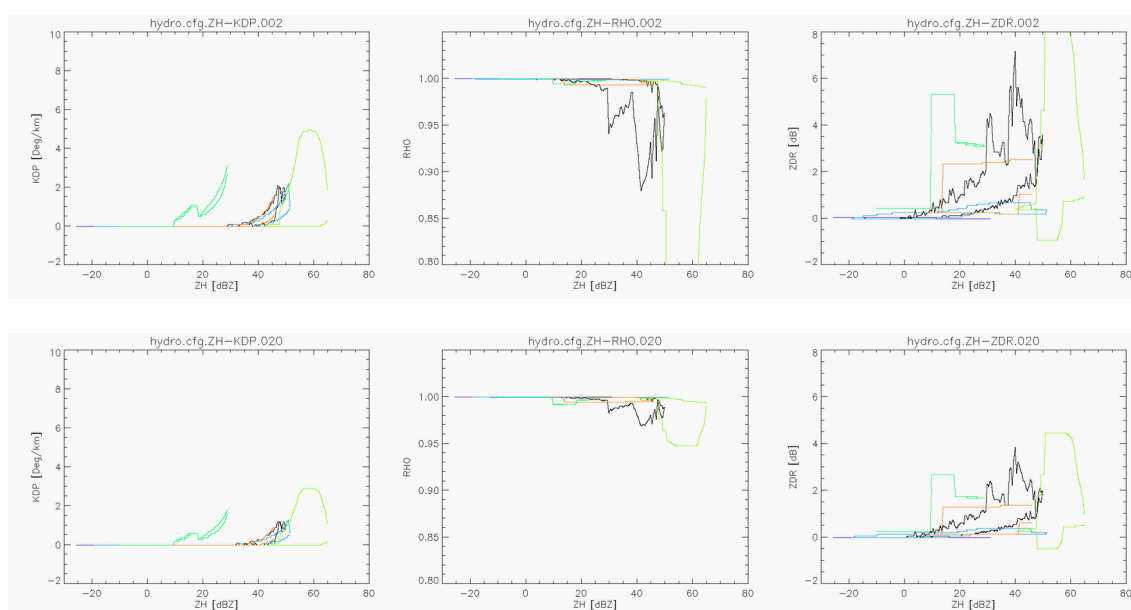


Fig. 32 Membership functions for the elevation 2 (0.4°) and 20 (40°) of the MeteoSwiss volumetric scan. Color code from black, bluish, green, orange: rain, snow, melting snow, ice crystals, hail/melting hail and graupel/melting graupel.

Chapter 12 **References**

- [1] Alduchov, O. A., and R. E. Eskridge, 1996: Improved Magnus Form Approximation of Saturation Vapor Pressure. *J. Appl. Meteor.* **35**, 601-609.
- [2] Al-Sakka, H., A.-A. Boumahmoud, B. Fradon, S. J. Frasier, and P. Tabary, 2013: A New Fuzzy Logic Hydrometeor Classification Scheme Applied to the French X-, C-, and S-Band Polarimetric Radars. *J. Appl. Meteor. Climatol.* **52**, 2328-2344.
- [3] Andric, J., M. R. Kumjian, D. S. Zrnic, J. M. Straka, and V. M. Melnikov, 2013: Polarimetric signatures above the Melting Layer in Winter Storms: an Observational and Modeling Study. *J. Appl. Meteor. Climatol.* **52**, 682-699.
- [4] Bailey, M. P., and J. Hallett, 2009: A Comprehensive Habit Diagram for Atmospheric Ice Crystals: Confirmation from the Laboratory, AIRS II, and Other Field Studies. *J. Atmos. Sci.*, **66**, 2888-2899.
- [5] Brandes, E. A., K. Ikeda, G. Zhang, M. Schönhuber, and R. M. Rasmussen, 2007: A Statistical and Physical Description of Hydrometeor Distributions in Colorado Snowstorms Using a Video Disdrometer. *J. Appl. Meteor. Climatol.*, **46**, 634-650.
- [6] Bringi, V.N., and V. Chandrasekar, 2001: *Polarimetric Doppler Weather Radar: Principles and Applications*. Cambridge University Press, 636 pp.
- [7] Cheng, L., M. English, and R. Wong, 1985: Hailstone size distributions and their relationship to storm thermodynamics. *J. Climate Appl. Meteor.*, **24**, 1059-1067.
- [8] Dolan, B., and S. A. Rutledge, 2009: A Theory-Based Hydrometeor Identification Algorithm for X-Band Polarimetric Radars. *J. Atmos. Oceanic Technol.*, **26**, 2071-2088.
- [9] _____, _____, S. Lim, V. Chandrasekar, and M. Thurai, 2013: A Robust C-Band Hydrometeor Identification Algorithm and Application to a Long-Term Polarimetric Radar Dataset. *J. Appl. Meteor. Climatol.*, **52**, 2162-2186.
- [10] Fabry, F., and W. Szyrmer, 1999: Modelling of the Melting Layer. Part II: Electromagnetic. *J. Atmos. Sci.*, **56**, 3593-3600.
- [11] Heymsfield, A. J., and C. D. Westbrook, 2010: Advances in the Estimation of Ice Particle Fall Speeds Using Laboratory and Field Measurements. *J. Atmos. Sci.*, **67**, 2469-2482.
- [12] Heymsfield, A. J., C. Schmitt, and A. Bansemer, 2013: Ice Cloud Particle size Distributions and Pressure-Dependent Terminal Velocities from In situ Observations at Temperatures from 0° to -86°C. *J. Atmos. Sci.*, **70**, 4123-4153.
- [13] Holt, A. R., 1984: Some factors affecting the remote sensing of rain by polarization diversity radar in the 3- to 35-GHz frequency range. *Radio Science*, **19**, 1399-1412.
- [14] Huang, G. J., V. N. Bringi, and M. Thurai, 2008: Orientation Angle Distributions of Drops after an 80-m Fall Using a 2D Video Disdrometer. *J. Atmos. Oceanic Technol.*, **25**, 1717-1723.
- [15] Ignaccolo, M., and C. De Michele, 2014: Phase Space Parameterization of Rain: The Inadequacy of Gamma distribution. *J. Appl. Meteor. Climatol.*, **53**, 548-562.

- [16] Jaffrain, J., and A. Berne, 2011: Experimental Quantification of the Sampling Uncertainty Associated with Measurements from PARSIVEL Disdrometers. *J. Hydrometeor.*, **12**, 352-369.
- [17] _____, and _____, 2012: Influence of the Subgrid Variability of the Raindrop Size distribution on Radar Rainfall Estimators. *J. Appl. Meteor. Climatol.*, **51**, 780-785.
- [18] Leinonen, J., D. Moisseev, M. Leskinen, and W. A. Petersen, 2012: A Climatology of Disdrometer Measurements of Rainfall in Finland over Five Years with Implications for Global Radar Observations. *J. Appl. Meteor. Climatol.*, **51**, 392-404.
- [19] Lim, S., V. Chandrasekar, and V. N. Bringi, 2005: Hydrometeor Classification System Using Dual-Polarization Radar Measurements: Model Improvements and In Situ Verification. *IEEE Trans. Geosci. Remote Sens.*, **43**, 792-801.
- [20] Liu, H., and V. Chandrasekar, 2000: Classification of Hydrometeors Based on Polarimetric Radar Measurements: Development of Fuzzy Logic and Neuro-Fuzzy systems, and In Situ Verification. *J. Atmos. Oceanic Technol.*, **17**, 140-164.
- [21] Marzano, F. S., G. Botta, and M. Montopoli, 2010: Iterative Bayesian Retrieval of Hydrometeor Content from X-Band Polarimetric Weather Radar, *IEEE Trans. Geosci. Remote Sens.*, **48**, 3059-3074.
- [22] _____, D. Scaranari, and G. Vulpiani, 2007: Supervised Fuzzy-Logic Classification of Hydrometeors Using C-Band Weather Radars, *IEEE Trans. Geosci. Remote Sens.*, **45**, 3784-3799.
- [23] Matrosov, S. Y., 2007: Modeling Backscatter Properties of Snowfall at Millimeter Wavelengths. *J. Atmos. Sci.*, **64**, 1727-1736.
- [24] _____, C. Campbell, D. Kingsmill, and E. Sukovich, 2009: Assessing Snowfall Rates from X-Band Radar Reflectivity Measurements. *J. Atmos. Oceanic Technol.*, **26**, 2324-2339.
- [25] _____, R. F. Reinking, R. A. Kropfli, and B. W. Bartram, 1996: Estimation of Ice Hydrometeor Types and Shapes from Radar Polarization Measurements, *J. Atmos. Oceanic Technol.*, **13**, 85-96.
- [26] Matzler, C. 2006: *Thermal Microwave Radiation: Applications for Remote Sensing*. The Institution of Engineering and Technology, 555 pp.
- [27] Mischenko, M. I., 2000: Calculation of the amplitude matrix for a nonspherical particle in a fixed orientation, *Appl. Opt.*, **39**, 1026-1031.
- [28] Mitra, S. K., O. Vohl, M. Ahr, and H. R. Pruppacher, 1990: A Wind Tunnel and Theoretical Study of the Melting Behavior of Atmospheric Ice Particles. IV: Experiment and Theory for Snow Flakes. *J. Atmos. Sci.*, **47**, 584-591.
- [29] Park, H. S., A. V. Ryzhkov, D. S. Zrnić, and K.-E. Kim, 2009: The Hydrometeor Classification Algorithm for the Polarimetric WSR-88D: Description and Application to an MCS. *Wea. Forecasting*, **24**, 730-748.
- [30] Pruppacher, H. R., and J. D. Klett, 1997: *Microphysics of Clouds and Precipitation*. 2nd Ed. Kluwer Academic Publishers, 954 pp.
- [31] Rasmussen, R. M., and A. J. Heymsfield, 1987: Melting and shedding of graupel and hail. Part I: Model physics. *J. Atmos. Sci.*, **44**, 2754-2763.
- [32] Ryzhkov, A. V., M. R. Kumjian, S. M. Ganson, and A. P. Khain, 2013: Polarimetric Radar Characteristics of melting Hail. Part I: Theoretical simulations Using Spectral Microphysical Modeling. *J. Appl. Meteor. Climatol.*, **52**, 2849-2870.

- [33] _____, M. Pinsky, A. Pokrovsky, and A. Khain, 2011: Polarimetric Radar Observations Operator for a Cloud Model with Spectral Microphysics. *J. Appl. Meteor. Climatol.*, **50**, 873-894.
- [34] Sekhon, R. S., and R. C. Srivastava, 1970: Snow Size Spectra and Radar Reflectivity. *J. Atmos. Sci.*, **27**, 299-307.
- [35] Straka, J. M., D. S. Zrnic, and A. V. Ryzhkov, 2000: Bulk Hydrometeor classification and Quantification Using Polarimetric Radar Data: Synthesis of Relations. *J. Appl. Meteor.*, **39**, 1341-1372.
- [36] Szyrmer W. and I. Zawadzki, 1999: Modeling of the Melting Layer. Part I: Dynamics and Microphysics. *J. Atmos. Sci.*, **56**, 3573-3592.
- [37] Thurai, M., G. J. Huang, V. N. Bringi, W. L. Randeu, and M. Schönhuber, 2007: Drop Shapes, Model Comparisons, and Calculations of Polarimetric Radar Parameters in Rain. *J. Atmos. Oceanic Technol.*, **24**, 1019-1032.